NASA CR-144013

RE- 505

RESEARCH ON METAL SOLIDIFICATION IN ZERO-G STATE

30 JULY 1975

RESEARCH DEPARTMENT

GRUMMAN AEROSPACE CORPORATION
BETHPAGE NEW YORK

Grumman Research Department Report RE- 505

RESEARCH ON METAL SOLIDIFICATION IN ZERO-G STATE

by

John M. Papazian

and

D.J. Larson, Jr.

Materials and Structural Mechanics
Research Department
Grumman Aerospace Corporation
Bethpage New York 11714

FINAL REPORT

(Reporting Period: 15 May 1973 to
30 July 1975)

Prepared under Contract NAS8-28604

for the

National Aeronautics and Space Administration
George C. Marshall Space Flight Center
Marshall Space Flight Center, Alabama 35812

Approved by: Charles E. Mack Jr.
Charles E. Mack, Jr.
Director of Research

ABSTRACT

The containerless solidification of several pure metals and metallic alloys has been studied in a low gravity environment. The tests were performed in the MSFC 4.2 s drop tower using a rapid wire melting apparatus designed and built for this purpose. Pure iron and nickel, and alloys of iron-nickel, iron-carbon, nickel-aluminum and tungsten-rhenium were all melted and solidified at a gravity level of approximately 10^{-4} g.

Interpretation of the results has led to an appreciation of the factors controlling the successful execution of this drop test experiment and to a delineation of the limits of applicability of the apparatus. Preliminary metallurgical evaluations are presented of the overall shapes, lattice parameters, surface microstructures, cross-sectional microstructures, solidification and transformation sequences, evaporative segregation, and localized solute redistribution observed in the low-gravity specimens. The effects of low gravity on metallic solidification are discussed with particular emphasis on observations of spontaneous undercooling and evaporative segregation in uncontained melts.

TABLE OF CONTENTS

LIST OF ILLUSTRATIONS

LIST OF ILLUSTRATIONS (Cont)

LIST OF ILLUSTRATIONS (Cont)

LIST OF TABLES

I. INTRODUCTION

The past several years have seen a significant increase in the number of experiments conducted in a low-gravity environment. The Skylab Space Processing experimental program was man's most extensive attempt to investigate the effect of a gravity-free environment on materials processing and the results of this program have generated many unanswered questions (Ref. 1). Because of the expense of manned space missions and the renewed interest in low-gravity research, there has been a reexamination of other, non-orbital, techniques for obtaining a low-gravity environment. The drop tower is unique among low-gravity research facilities because it is the only facility which allows rapid, repetitive experimentation. It is also relatively inexpensive and provides a low gravity level of about 10^{-4} g. However, a great liability of the tower is the short duration of the low-gravity interval. Current facilities in the USA include the MSFC 4.2 s tower and the LeRC 2.2 s and 5/10 s towers. There is also considerable interest in drop towers elsewhere; a 200 m 6.3 s facility is under construction in West Germany (Ref. 2) and a tower is operational in the USSR (Ref. 3).

This document is the final report of a program of research on low gravity metallic solidification that was conducted in the MSFC drop tower under partial support of NASA contract NAS8-28604 MOD. 6. Solidification is thought to be one of the areas of metallic processing that may profit from the low gravity environment (Ref. 4). The initial phase of this program involved the design and construction of a rapid melting apparatus and some preliminary experimentation (results were reported previously in Ref. 5). This report describes our subsequent attempts to use the apparatus to study the effects of low gravity on metallic solidification. Specific goals of this phase of the project were: a) an investigation of evaporative segregation in freely floating liquid metal alloys and, b) a study of the possibility of obtaining undercooling in containerless melts in low-g. During the course of this project we became aware that scientists studying lunar and meteoritic magnetic mateials were in need of specimens solidified in low gravity under controlled conditions. By a happy coincidence, one of the alloys chosen for our investigation was well-suited to these studies; thus, we have provided some specimens to Dr. P. Wasilewski of NASA-GSFC for magnetic measurements.

II. EXPERIMENTAL TECHNIQUE

A. Apparatus

The apparatus constructed for this investigation is designed for use in a drop tower or sounding rocket and allows one to rapidly melt a length (up to 6 cm) of wire (approximately 0.2 to 2 mm diameter). The molten wire decays to spheres which then solidify while floating freely. Melting is begun 250 ms after initiation of the drop test and the molten specimens solidify while in free fall during the remainder of the low-gravity interval (approximately 3.5 s total). The experiment is performed in a static vacuum. A continuous visual record of the experiment is made on motion picture film (Kodak Ektachrome Type 7242) with a Milliken camera running at 128 frames per second. The sample current, sample voltage, gravity level, and chamber pressure are monitored and continuously recorded by the drop tower telemetry systems. At the conclusion of the test the samples are collected for laboratory analysis. The apparatus is described in detail in a previous report (Ref. 5) and in the service manual previously submitted to MSFC. It has performed successfully in several dozen low-gravity tests in the MSFC 300-foot drop tower. Several modifications have been made since the original service manual was written; these have been described in two addendums subsequently submitted to MSFC.

B. Temperature Measurement

The color film record of the experiment serves as the means for temperature measurement. After film processing, the image is analyzed using a recording microdensitometer. The observed optical densities are then converted to temperatures using an analysis technique that will be explained below. Despite the variable and nonlinear nature of film as a recording medium, this technique is well-suited to the experiment. It provides a complete spatial and chronological history of the specimen temperature while requiring no connections to the sample. Thus, we have an independent record of the history of each sphere.

In its simplest form the analysis technique consists of first photographing a tungsten filament preset at various temperatures and establishing a correlation between optical density (read from the film) and temperature and then using this correlation to deduce the specimen temperature, frame-by-frame, from films of the low-gravity tests. The accuracy of this procedure is much improved by including, in the field-of-view of the low-gravity test, a reference filament whose temperature is preset using an optical pyrometer. The presence of the reference filament in each frame permits adjustment of the measured values for

uncontrolled fluctuations such as camera speed, film development, etc. This analysis procedure is based upon relative brightness and is fully described in Ref. 6. We measure the "relative brightness" temperature for each of the three emulsions of the color film; thus we have three data points for each location. One of the major limitations of this technique is its dependence upon the spectral emissivity of the material. The spectral emissivity is a function of the material, its state, temperature, and wavelength of the radiation. The variation in emissivity with these parameters is not trivial; for instance, the emissivity of copper at 650 nm varies from 0.1 to 0.7 depending on whether it is solid, liquid, or oxidized (Ref. 7). To circumvent this limitation, we have developed the two-color analysis technique described below.

Two-color optical pyrometry compares the radiation intensity at two wavelengths; the temperature is determined by this ratio and Planck's Law. The emissivity cancels in the first order. We have applied this principle to our measurements by forming binary ratios of the radiation intensities determined at 630 nm, 530 nm, and 440 nm. Thus, we still have three temperature determinations per sample per frame. This analysis procedure represents a significant advance and is described more fully in Ref. 8. An example of a thermal history obtained in this manner is shown in Fig. 1. Each point is the average of the three uncorrected two-color values. The curve shows the sequence of wire heating, wire melting, cooling to the solidification temperature, T_S, solidification, and subsequent cooling.

C. Simulations

At the beginning of this investigation little information was available on the conditions necessary for the formation of spheres from wire by rapid resistance heating. A vacuum bell jar was used to study the process in our laboratory, both AC and DC power supplies were employed and efforts were made to provide circuitry with an internal resistance equal to that of the experimental package.

Simulations were also performed on a computer. A program was written (Ref. 9) which faithfully models the heating and melting process and calculates the instantaneous voltage, current, and sample temperature as a function of time.* It also calculates the total time required to heat the specimen from the starting temperature to the melting

*This program is available to interested parties.

point and then to completely melt the wire. Input variables are source voltage V, source resistance R2, specimen length L, specimen diameter d, starting temperature T_o, melting point T_m, room temperature resistivity ρ_o, temperature coefficient of resistivity α, specific heat C_p, heat of fusion ΔH, density ρ, and total emissivity ϵ. Values for these variables were obtained from the literature. It is assumed that heat loss is due solely to radiative transfer; thus, conduction through the grips has been neglected. This program has been very informative in providing a rapid method for evaluating the critical parameters for successful wire melting and, hence, sphere formation.

D. Specimen Analysis

The specimens formed during the drop were collected after each run. The analysis procedure included: 1) low-power optical examination and macrophotography; 2) X-ray analysis using a Gandolphi camera (Ref. 10); 3) surface microstructure analysis in the scanning electron microscope; 4) surface composition analysis using energy dispersive X-ray analysis (EDAX); 5) metallographic examination of polished cross-sections; and 6) electron microprobe analysis.

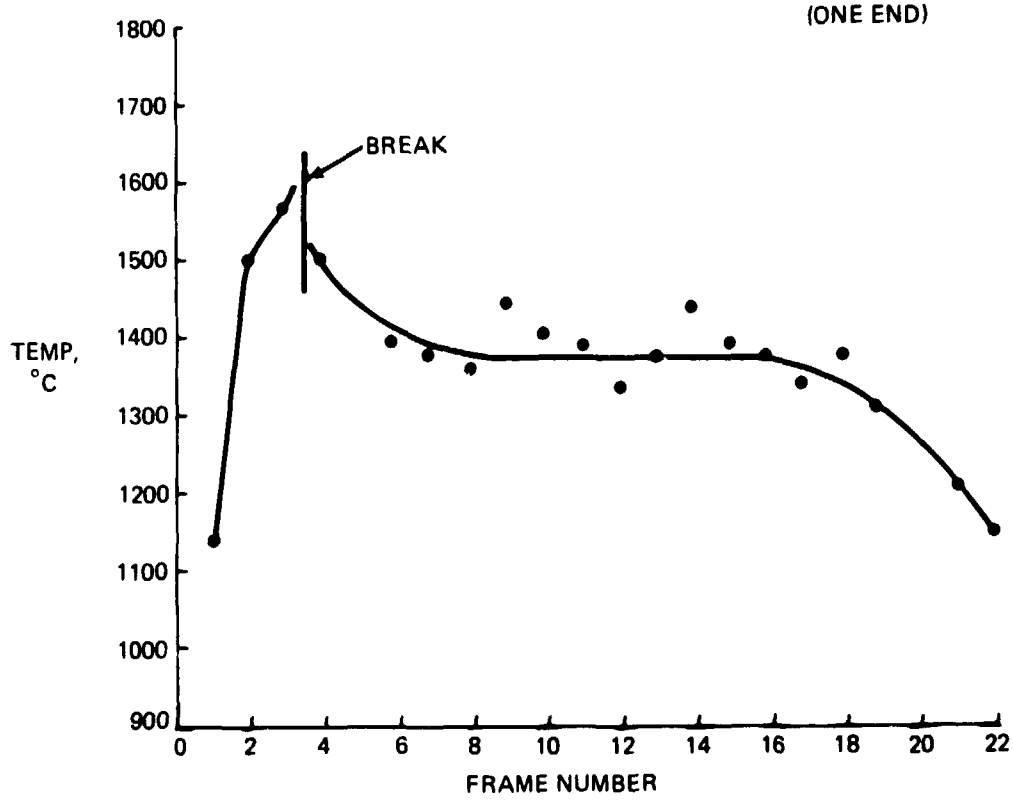

Fig. 1 Two-Color Temperature: Time History of Specimen 221 (Fe-26% Ni)

III. RESULTS

Since the last reporting period we have made 26 additional low-gravity tests during two one-week visits to MSFC (2-6 December 1974 and 20-24 January 1975). Spherical specimens, melted and solidified in low gravity, were produced in 16 of these tests. We experienced less than a 100 percent rate of success mainly because of minor equipment malfunctions, including loosened or corroded contacts, broken batteries, and too much tension in the specimen mount. Our original goal in this contract was to produce low gravity specimens of Ni-5% Al and Fe-25% Ni. We have produced at least ten specimens of each of these materials, as well as specimens of Fe-5% Ni, Fe-9% Ni, Fe-15% Ni, Fe-21% Ni, W-3% Re, W-25% Re, chromel, pure iron, and titanium. In each case the starting material was a 5 cm long segment of 0.5 mm diameter wire. Pure nickel and 1090 steel specimens were produced in the initial phase of the contract and should be added to this list. The average yield of a successful drop was approximately 5 spheres, in addition to the two balled ends formed on the pieces of wire that were held in the grips. (These balled ends are called sting-mounted specimens in the following discussion.) The diameter of the spheres varied from approximately 0.6 to 2 mm; the distribution of diameters was not analyzed. Figure 2 is a macrograph of the Fe-9% Ni specimens obtained in run 20; this was one of the most successful drops. Table 1 is a listing of the various materials that we have successfully melted and solidified in low gravity. The number, N, of spherical specimens obtained in each run (excluding the sting-mounted specimen) is shown in the fourth column.

A. Criteria for Sphere Formation

Successful specimen production in this experiment is contingent upon uniformly heating the wire to its melting point and forming a completely molten column of liquid metal in mechanical equilibrium. This column becomes geometrically unstable and breaks up into spheres in order to minimize surface energy. The time required for transformation of the liquid column into spheres is typically less than 3 ms for the conditions used in this experiment (Ref. 11, 12). Although the melting and sphere formation process seems straightforward, numerous problems were encountered in consistently producing spheres. In general, it was found that wires with diameters greater than about 0.5 mm did not produce useful specimens. In addition, erratic results were often observed even when working with the same material and wire size.

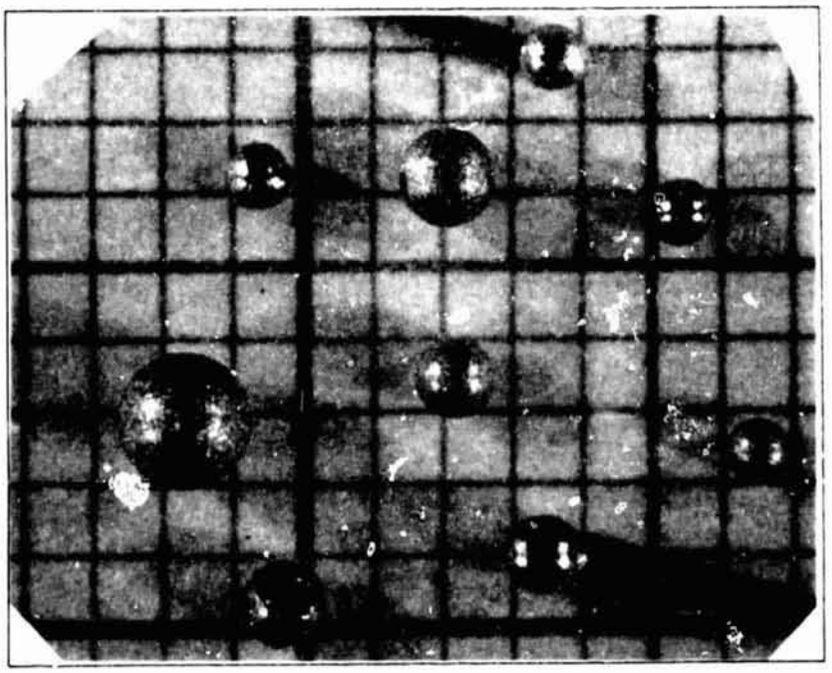

NOTES:

1. EACH SMALL DIVISION IS ONE MM.
2. ONE SPECIMEN (d ≅ 1.3 MM) IS MISSING.

Fig. 2 Macrograph of Specimens From Run 20 (Fe-9% Ni)

TABLE 1. CHARACTERISTICS OF SUCCESSFULLY MELTED MATERIALS

Material	Run	Date	N	Observed Values		Calculated Values	
				$\bar{I}$ (A)	t_m (ms)	$\bar{I}$ (A)	t_m (ms)
Ni	T-2	14 Feb 73	7	200	25	120	32
Ni	T-3	15 Feb 73	14	200	25	120	32
Steel, 1090	T-4	15 Feb 73		100	50	61	58
Ni	2T-11	30 Mar 73	8	*	25	120	32
Ni - 5% Al	1-1	19 Mar 74	1	100	75	105	38
Ni - 5% Al	2-1	20 Mar 74	2	*	25	105	38
Ni - 5% Al	3-1	21 Mar 74	4	130	25	105	38
Ni - 5% Al †	1	3 Dec 74	2	115	24	105	38
Ni - 5% Al †	9	4 Dec 74	2	111	24	105	38
Fe - 21% Ni	13	5 Dec 74	5	75	44	80	43
Fe - 5% Ni	14	5 Dec 74	1	90	44	80	43
Fe - 9% Ni	20	6 Dec 74	8	90	52	80	43
Fe - 26% Ni	22	6 Dec 74	9	78	49	80	43
Fe - 15% Ni	23	6 Dec 74	9	78	49	80	43
Fe - 15% Ni	34	21 Jan 75	4	*	44	80	43
Fe - 5% Ni	35	21 Jan 75	6	*	44	80	43
Fe - 26% Ni	36	22 Jan 75	3	*	40	80	43
Fe - 9% Ni	39	22 Jan 75	6	95	48	80	43
Ta ‡	45	23 Jan 75	2	100	48	60	74
Pt ‡	46	23 Jan 75	9	175	24	106	29
Chromel	47	23 Jan 75	9	63	32	82	47
W - 25% Re	50	23 Jan 75	6	100	60	105	52
W - 3% Re	53	23 Jan 75	1	95	60	104	56
Fe	54	24 Jan 75	8	71	48	100	32
Ti	56	24 Jan 75	7	72	40	300	13

† new batch of material
‡ one gravity simulation
* not measured

One source of trouble was found to be the chamber pressure. This was investigated in our laboratory using a dynamically pumped bell jar with a variable transformer power supply to melt 5 cm long by 0.05 cm diameter constantan (approximately, 60% Cu 40% Ni) wire. The results are shown in Fig. 3 where the number of spheres obtained is plotted as a function of applied voltage for three chamber pressures. The existence of a threshold voltage for sphere formation had previously been observed (Ref. 5); however, when melting in air, a cutoff voltage was also observed. It is possible that a cutoff voltage also exists for the other pressures. This result is a possible explanation for the poor yield of the second (March 1973) series of drops, as it shows that there exists a range of power inputs for successful sphere formation, and this range narrows as the pressure approaches atmospheric. Thus, uncontrolled variations in the chamber pressure can influence sphere yield. In order to control this problem in our (static) vacuum chamber a large cold trap and pressure telemetry system were added.

Valuable insight into the wire melting and sphere formation process was obtained by modeling the event mathematically. The computer program (described briefly in Section II and available from the authors, Ref. 9) was initially used to calculate the total time to melt, t_m, and the average current, $\overline{I}$, for the various materials used in the drop tests. These calculated values are shown in columns 7 and 8 of Table 1 and are to be compared to the values read from oscillograph traces of the drop tower telemetry shown in columns 5 and 6. The agreement is not perfect, but it is certainly good enough to inspire confidence in the physical validity of the model, particularly since there are no adjustable parameters. The calculated values were all obtained using L=50 mm, d = 0.5 mm, V = 23 V, and R2 = 0.027 Ω. These are the nominal values used tn the actual experiment. Values of the other variables were taken from handbooks for the particular materials.

The program was also used to investigate the effect of variations in d, L, and R2 on the time to melt. Results of these calculations are shown in Fig. 4, 5, and 6. In each case the variable in question was varied while holding the others constant at their nominal values for our apparatus. In Fig. 4 we see that increasing the specimen diameter causes a rapid increase in the time required for melting. The rate of increase varies with the particular material in question. Calculations were made for copper, silver, gold, platinum, iron, nickel, titanium, tantalum, tungsten, iron-25% nickel, nickel-5% aluminum, tungsten-25% rhenium, chromel and nichrome. In the graphs we do not show lines for all of the materials investigated, but we have chosen representative materials that display both extremes of behavior, i.e., the least and most sensitive to diameter. Likewise, increasing the wire length increases the time to melt, as shown in Fig. 5. It is thought that the sharp dropoff in t_m for $L \leq 2.5$ cm is physically unrealistic due to our having failed to include

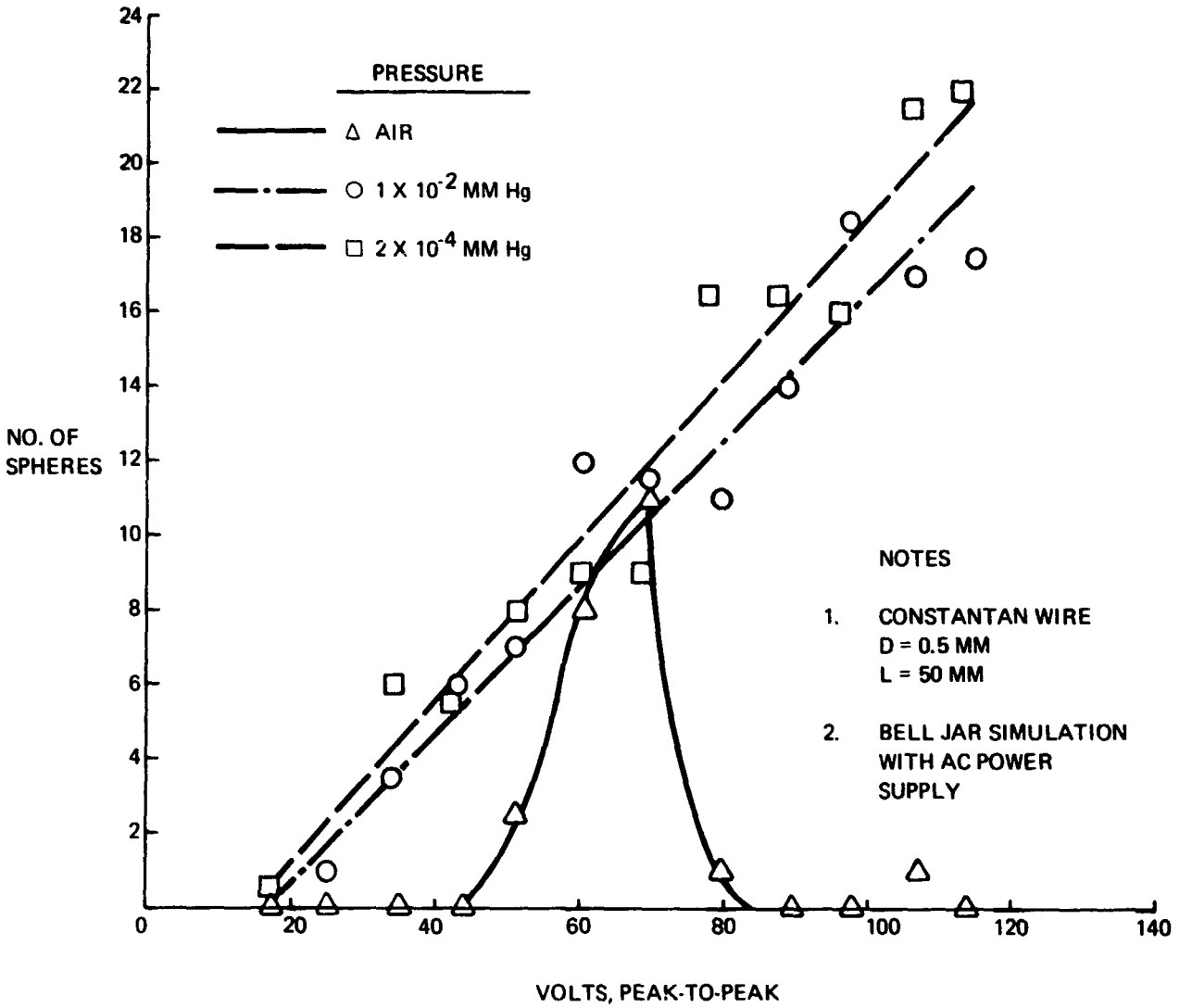

Fig. 3 Number of Spheres as a Function of Applied Voltage and Chamber Pressure

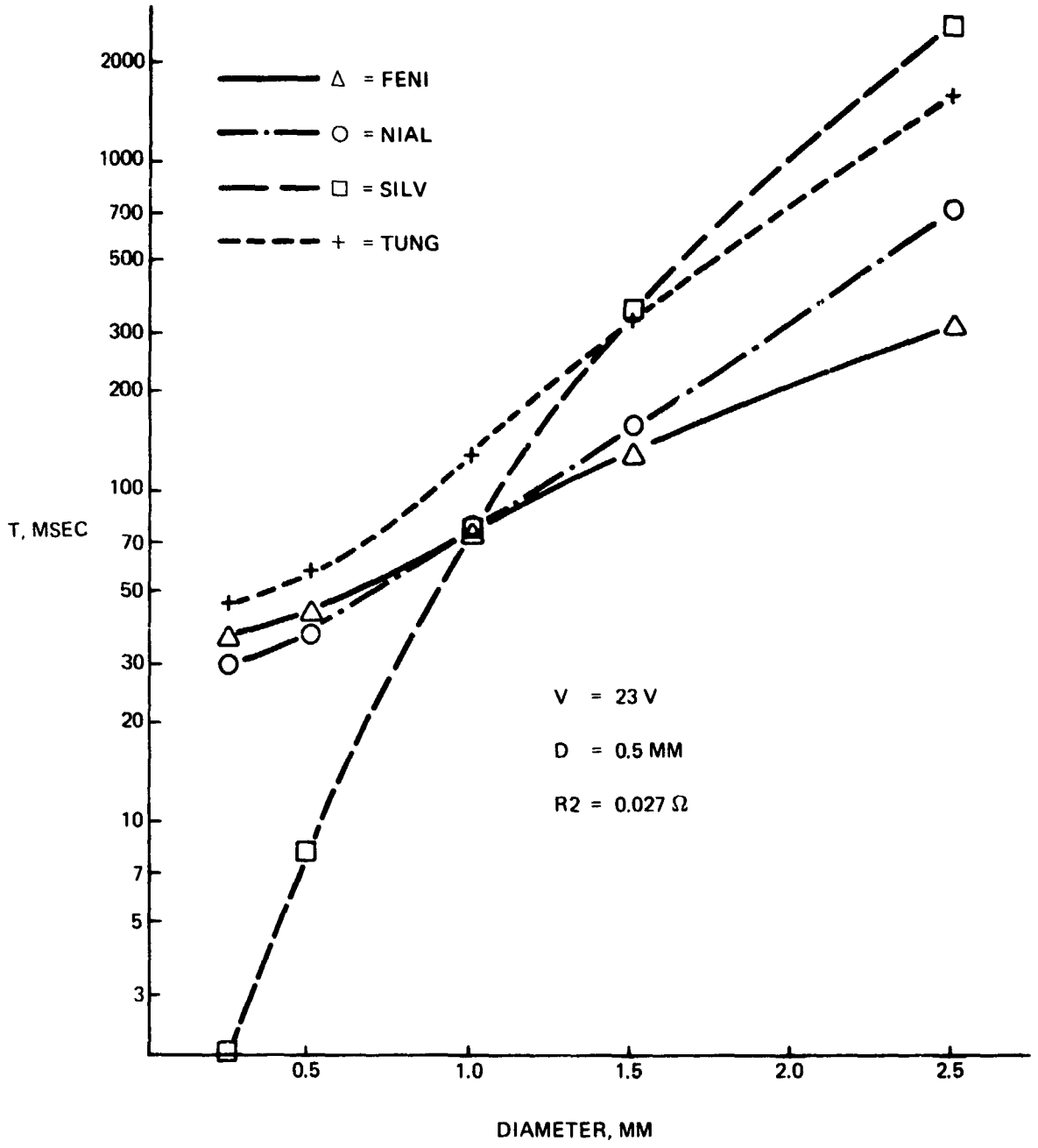

Fig. 4 Time to Melt as a Function of Specimen Diameter From EPLOD 6

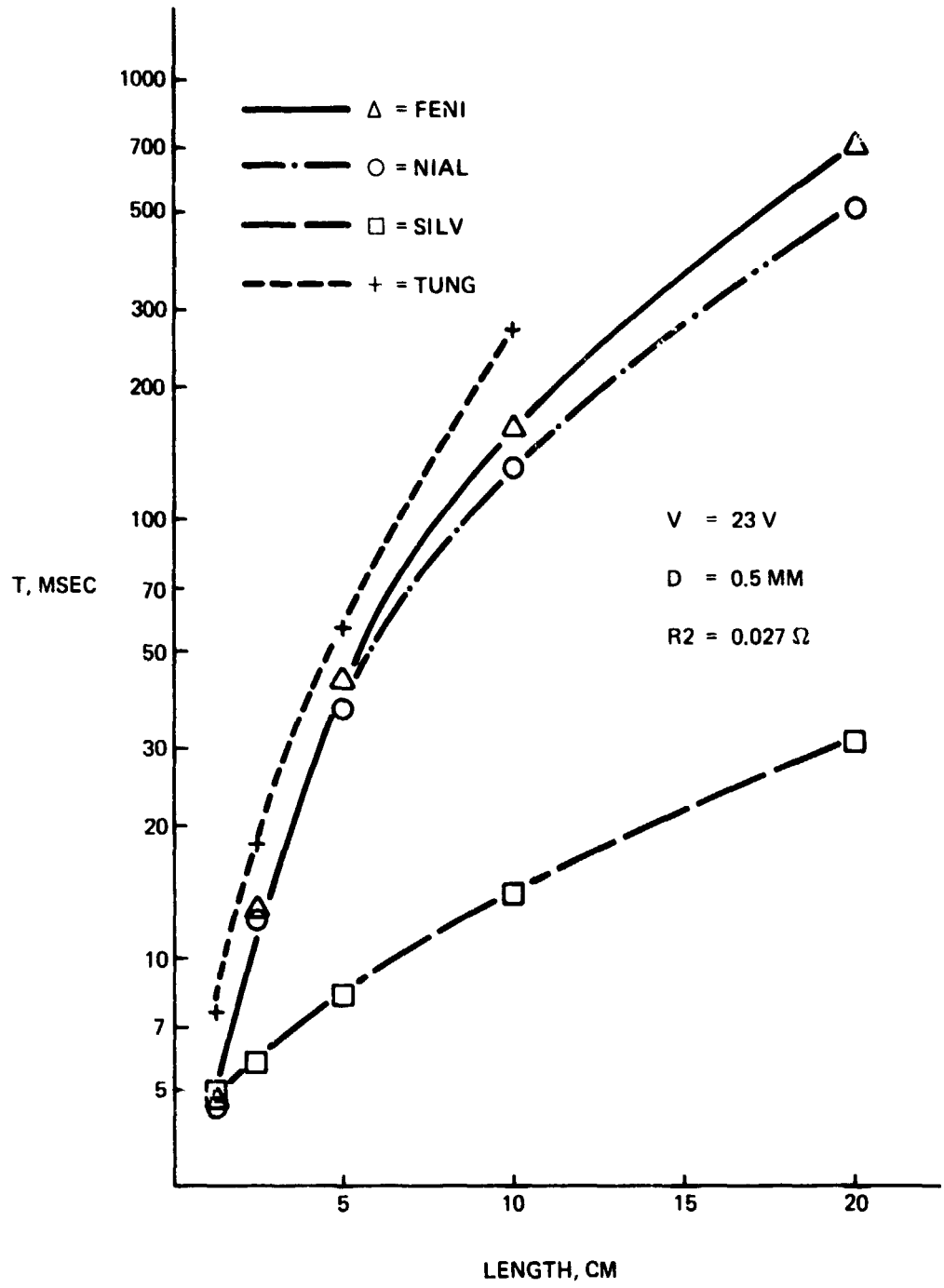

Fig. 5 Time to Melt as a Function of Specimen Length From EPLOD 6

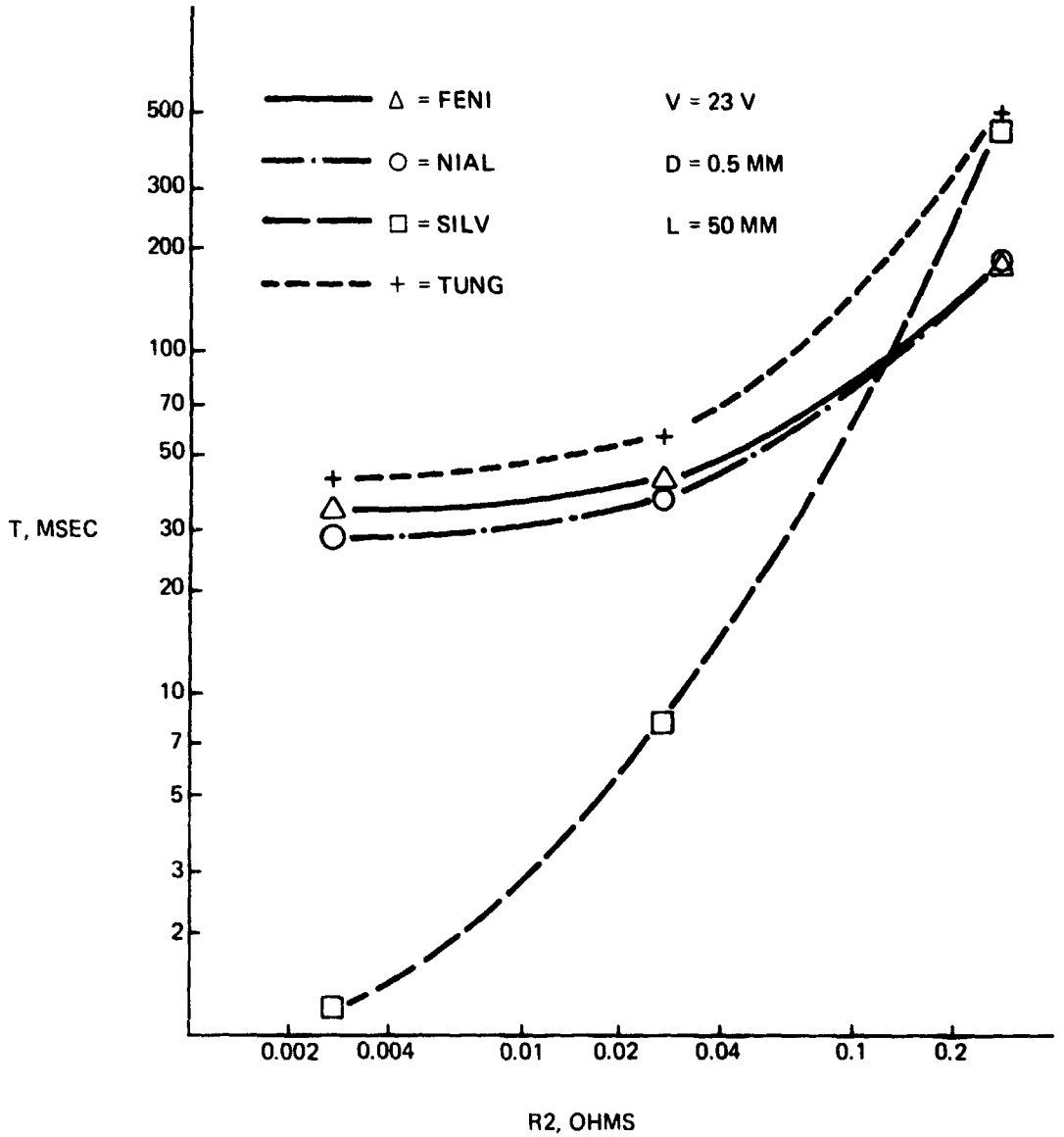

Fig. 6 Time to Melt as a Function of Internal Resistance From EPLOD 6

thermal losses due to conduction through the grips. These losses will become proportionally more significant as L decreases; we therefore discount this trend and expect that the curves will flatten out and possibly even rise as L approaches zero. Decreasing the source resistance (i.e., increasing the maximum short-circuit current) lowers t_m drastically for high conductivity pure materials but has little effect on poorer conductors, Fig. 6. This is due to the impedance match between the source and specimen; thus these remarks hold only for the particular wire length and diameter used in this calculation.

In order to more fully utilize these results, we propose as a hypothesis that a necessary condition for successful production of fully molten spheres is the melting of the wire in approximately 50 ms or less. This is not thought to be a sufficient condition for a successful melt nor can we offer a proof of its validity. However, we find it useful in ordering our ideas about the sphere-forming process. We justify this hypothesis as follows.

Empirically, we observe that for $d \simeq 0.5$ mm we have a high rate of success; from Fig. 4 we see that for most materials $t_m \leq 50$ ms when $d \leq 0.5$ mm. Further, most of the successful drop tests occurred with $t_m \simeq 50$ ms (see Table 1). In addition, our calculations show that the time required to heat the wire to its melting point is typically only 2/3 of the total time to melt, while 1/3 of the time is spent in providing the latent heat of fusion. Thus, for a significant fraction of the melting process the metal is in a partially liquid, mushy state and can support practically no stress. This problem is exacerbated in alloys with a wide solidification range. It is thought that this interval must be traversed rapidly in order to achieve a completely molten liquid column which can then form spheres. The mushy condition is susceptible to perturbations; any perturbation which leads to a premature loss of electrical continuity in the specimen will result in an unsatisfactory melt. There are several possible sources of such perturbations, including small mechanical accelerations, electromagnetic forces, and surface tension. For instance, if the wire is under tension it could be literally pulled apart before it is completely molten; we have observed this type of failure in motion pictures of some of our runs. Also, if residual stresses were present small accelerations may have been imparted to the sample during warmup. Thermal expansion could cause sample motion. The electromagnetic field due to sample current could cause an acceleration of the sample if it were not perfectly straight. Finally, failure could occur at a local hot spot due to unduloid formation and premature pinching off. All of these processes are possible sources of failure; thus, it is thought that dwelling in the mushy state must be avoided.

Conversely, the specimen should not melt too quickly. In exploding wire studies (Ref. 13) melting generally takes place more rapidly, but the heating rate is so high that significant overshooting of the melting point occurs to the extent that boiling, vaporization, and plasma formation are observed. This is undesirable in our experiment since vaporization will lead to changes and gradients in the composition of alloys (Ref. 14), unnecessarily complicating interpretation of the solidification process. On the basis of these considerations we postulate that for successful sphere production the wire should be heated and melted in less than 50 ms and it should be isolated from any perturbations, particularly while it is in the mushy state.

Using this hypothesis as a guide, we see from Fig. 4 that it is unlikely that wires with $d > 0.5$ mm can be successfully melted in our apparatus, no matter what material we choose. In addition, if the wire length is greater than 5 cm we will be unsuccessful, except for high conductivity pure metals such as silver (see Fig. 5). Further, replacing the batteries with batteries of higher internal resistance (lower short-circuit current) is not advisable; and using lower internal resistance batteries is unnecessary (Fig. 6).

In order to generate larger diameter specimens using this apparatus, there is some possibility that optimization of L and R2 for the particular material would lead to successful results for moderately larger wire diameters. However, it is thought that a different type of power supply (e.g., capacitor discharge) incorporating a facility for matching the rate of energy input to the wire dimensions and material characteristics would be desirable.

B. Solidification Time

The time required to solidify individual specimens was measured from the film record of the experiment. The solidification time, t_s, was obtained by counting the number of frames between the formation of the spheres and the end of the solidification plateau. This number was divided by 128, the nominal framing rate of the camera, in order to obtain the solidification time. Thus, the specimen shown in Fig. 1 solidified in approximately 0.12 s. Solidification times measured in this manner are listed in Table 2 for a number of specimens. The solidification time should be a linear function of the specimen diameter; however, we observe fairly wide variations. For freely floating specimens of about 1 mm diameter the solidfication time varies from 0.2 to 0.8 s. The sting-mounted specimens cool more quickly than the freely floating specimens because of thermal conduction through the support and are not considered in the following discussions.

TABLE 2. CALCULATED AND OBSERVED SOLIDIFICATION TIMES OF VARIOUS SPECIMENS

Material	Specimen	P (torr)	D (mm)	t_s, obs (s)	t_s, calc (s)
Ni - 5% Al	1-1	$> 10^{-2}$	0.9	0.2	.64 *
Ni - 5% Al	1-1A	$> 10^{-2}$	1.0 †	0.77	–
Ni - 5% Al	3-1A	3×10^{-4}	1.1	1 41	2.83
Ni - 5% Al	3-1	3×10^{-4}	0.9 †	0.25	–
Ni - 5% Al	3-1P	3×10^{-4}	0.9 †	0.59	–
Ni - 5% Al	9B	$> 10^{-2}$	1.0	0.8	.72 *
Fe - 5% Ni	35A	4×10^{-4}	1.8	0.8	3.79
Fe - 5% Ni	35D	4×10^{-4}	1.4	2.52	2.94
Fe - 5% Ni	35B	4×10^{-4}	1.0 †	0.12	–
Fe - 5% Ni	35G	4×10^{-4}	1.0 †	0.12	–
Fe - 9% Ni	20D	$< 10^{-1}$	1.1 †	0.2	–
Fe - 9% Ni	20E	$< 10^{-1}$	0.9 †	0.2	–
Fe - 15% Ni	23D	$> 10^{-2}$	1.0	0.24	.60 *
Fe - 15% Ni	23J	$> 10^{-2}$	0.9 †	0.16	–
Fe - 15% Ni	23K	$> 10^{-2}$	0.6 †	0.09	–
Fe - 15% Ni	34C	2×10^{-4}	1.8	0.52	3.79
Fe - 15% Ni	34E	2×10^{-4}	1.1	0.8	2.32
Fe - 15% Ni	34B	2×10^{-4}	0.9 †	0.14	–
Fe - 15% Ni	34F	2×10^{-4}	1.5 †	0.36	–
Fe - 26% Ni	22E	$> 10^{-2}$	1.2	0.55	.72 *
Fe - 26% Ni	22B	$> 10^{-2}$	1.4	0.62	.84 *
Fe - 26% Ni	22J	$> 10^{-2}$	0.9 †	0.12	–
Fe - 26% Ni	36C	3×10^{-4}	1.2	0.2	2.53
Fe - 26% Ni	36B	3×10^{-4}	1.4 †	0.13	–

† Sting mounted
* for P = 1 torr

It is interesting to know what solidification times would be expected; these times can be estimated in a straightforward manner. For an empirical estimate we can use the data of Joly and Mehrabian, Ref. 15. They measured the dendrite element spacing of maraging VM300 steel steam-atomized powders and compared the measured spacings to spacings observed in ingots cooled at controlled rates. They used the equation of interface controlled heat flow which allows for loss by radiation and conduction (Ref. 16) and assumed that the rate of heat extraction during solidification was the same as during subsequent cooling. Upon equating the solidification time multiplied by the rate of heat loss to the heat of fusion of the sample, they obtain for a spherical specimen

$$t_s = \frac{D \rho H}{6h(T_m - T_o)} \tag{1}$$

where

D = specimen diameter (cm)
ρ = density of the solid (gm cm^{-3})
H = heat of fusion (cal gm^{-1})
h = heat transfer coefficient (cal $cm^{-2} s^{-1} K^{-1}$)
T_m = melting temperature (K)
T_o = temperature of the medium (K)

Using the parameters for Fe - 25% Ni

$$\rho = 8 \text{ gm cm}^{-3}$$
$$H = 72 \text{ cal gm}^{-1}$$
$$T_m - T_o = 1400 \text{ K}$$

and the value of $h = 3.9 \times 10^{-3}$ cal cm^{-2} s^{-1} K^{-1} determined by Joly and Mehrabian for this alloy, we have

$$t_s = 17.5D \tag{2}$$

Thus a 0.1 cm diameter sphere should solidify in 1.75 seconds if cooling were the same as in the steam atomization process.

We can also make other estimates. In Ref. 17 the solidification time was calculated for heat loss by radiation and evaporation. For radiative cooling we have

$$t_s = \frac{\rho H D}{6\sigma \epsilon T_m^4} \tag{3}$$

where

σ = Stefan-Boltzman constant, 1.35×10^{-12} cal $cm^{-2} s^{-1} K^{-4}$

ϵ = total emissivity

For Fe-25% Ni this becomes

$$t_s = \frac{8}{\epsilon} D \tag{4}$$

Similarly, for evaporative cooling we calculate

$$t_s = \rho \frac{HD}{6GH_v} \tag{5}$$

where

G = evaporation rate (gm cm^{-2} s^{-1})

H_v = heat of vaporization (cal gm^{-1})

Using values of G from Ref. 18, we have

$$t_s = 100\ D \tag{6}$$

for Fe-25% Ni. Likewise, we can calculate the solidification time due to gaseous conduction. Using the equations given in Ref. 18 for free-molecule conductivity (for P 10 torr) we obtain

$$t_s = \frac{pVH}{A\alpha\Lambda_o P (273/T_m)^{1/2} (T_m - T_o)} \tag{7}$$

where

V = sample volume

A = surface area

α = accommodation coefficient

Λ_o = free molecule heat conductivity

P = pressure (torr)

With the value of Λ_o for air (Ref. 18) and estimating the accommodation coefficient as 0.9 (see Ref. 19), we obtain

$$t_s = \frac{17.8\ D}{P} \ . \tag{8}$$

Assuming that the three different mechanisms of heat loss operate in parallel, we obtain a minimum solidification time for Fe-25% Ni:

$$t_s = \frac{D}{0.01 + 0.125\epsilon + 0.056P} \tag{9}$$

The analogous expression for Ni-5% Al is

$$t_s = \frac{D}{0.12\epsilon + 0.003 + 0.041P} \tag{10}$$

Figure 7 is a plot of the solidification time for Fe-25% Ni as a function of pressure for a specimen of 0.1 cm diameter. Two different values of the emissivity are used; 0.3 is a typical value for a clean iron surface and 0.8 is typical of an oxidized surface (Ref. 20). The accommodation coefficient, α , in the expression for gaseous conduction is also dependent upon the state of the sample surface. Values of the order of 0.9 are observed for typical engineering surfaces; for atomically clean surfaces α may drop to 0.05 or less. We prefer the higher value since, if there is enough gas present to cause significant heat loss, there is also enough gas present to oxidize the surface. Figure 7 shows that, for pressures less than 0.1 torr, radiative transfer is the dominant heat loss mechanism and the solidification time is relatively constant at 2.6 s for a clean specimen and 1 second for an oxidized specimen. When the chamber pressure rises above 0.1 torr, gaseous conduction becomes important and the solidification time decreases. Our expression for gaseous conduction is not valid for P> 10 torr; thus, for P> 10 torr, t_s will not continue to decrease as rapidly as shown in Fig. 7. Evaporative cooling is never very important under these conditions for the materials we used. There is good agreement between our calculations and those of Joly and Mehrabian.

Using Eq. 9 and 10 we can calculate the expected solidification time of a sphere as a function of its diameter, emissivity, and chamber pressure. Empirically we observe that for pressures in the 10^{-4} torr range the specimens are bright and shiny, whereas for greater chamber pressures the specimens are dull and oxidized. Thus, in our calculations we use $\epsilon = 0.8$ for $P > 10^{-3}$ torr and $\epsilon = 0.3$ for $P < 10^{-3}$ torr. The calculated solidification times are shown in column 6 of Table 2. It is seen that while in some cases the agreement is good, in other cases the observed solidification time is significantly less than the predicted time. No explanation can be offered for this at the present time.

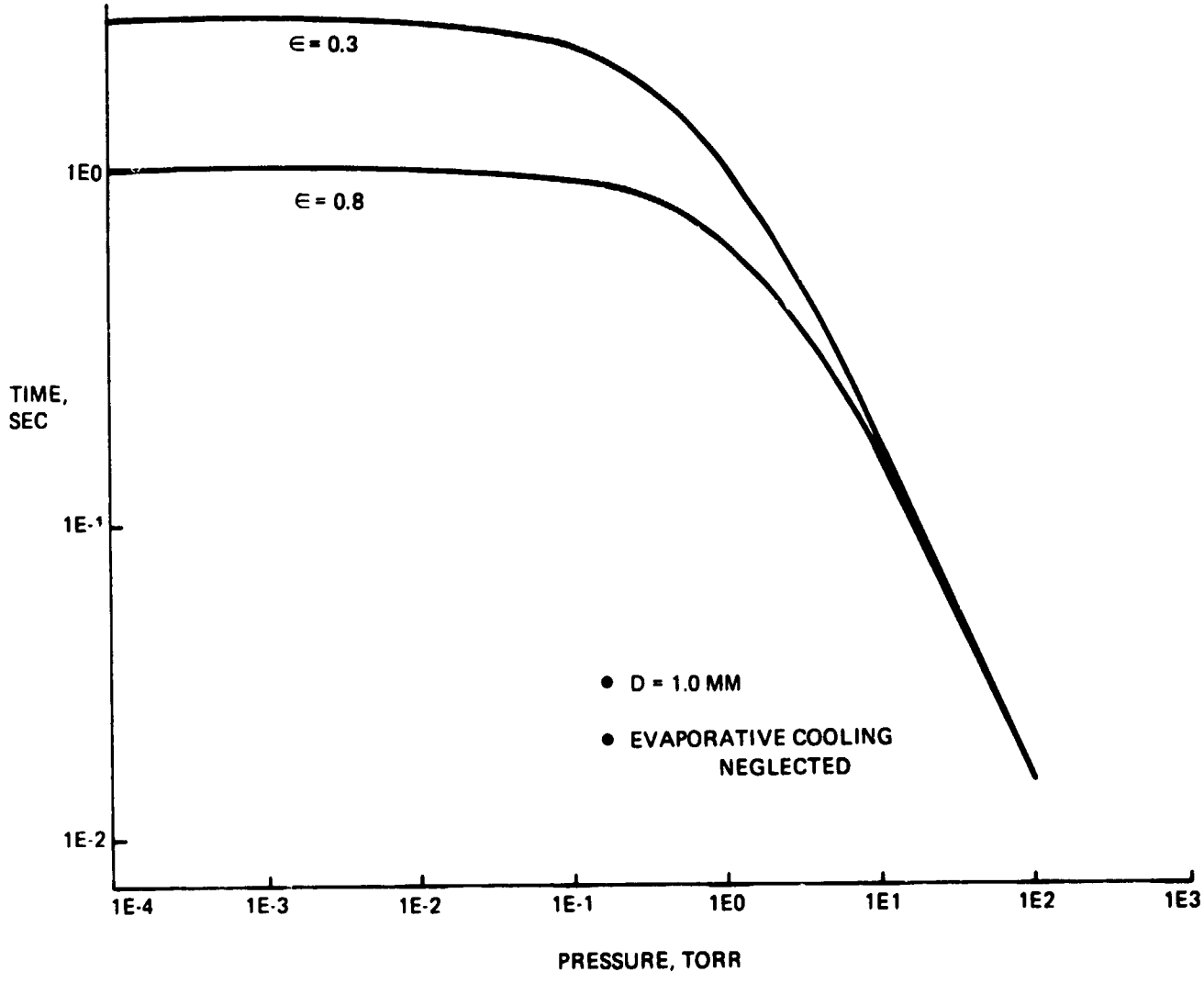

Fig. 7 Solidification Time as a Function of Chamber Pressure From Equation 9

C. X-ray Studies

Crystal structures and lattice parameters of specimens of iron, iron-nickel, and nickel-aluminum were determined using a Gandolfi X-ray camera with CoK_{α} radiation. This camera rotates the specimen around two axes and is ideally suited to our small spherical polycrystalline specimens. It produces a film which is identifical to a Debye-Scherrer pattern with significantly less spottyness for equivalent grain sizes or textures. Values of the lattice parameter as a function of $\sin^2\theta$ were extrapolated linearly to $\sin^2\theta = 1$ to get a_o (Ref. 21). The results for nickel and nickel-aluminum are $a_o = 0.3521$ nm and $a_o = 0.3531$ nm, respectively. The handbook value for nickel is given as 0.3524 nm; our results differ from this by 0.1 percent. The value of the lattice parameter of Ni-5% Al solidified in one gravity is 0.3524 nm (Ref. 22), a difference of 0.3%.

All of the iron-nickel alloys studied were found to be bcc with no evidence of retained austenite. The values of a_o obtained on the iron and iron-nickel specimens are shown in Fig. 8. We obtained $a_o = 0.2875$ nm for pure iron while the handbook value is 0.2866 nm, a difference of 0.9 pm or 0.3 percent. The difference is thought to be due mainly to the relatively large specimens used ($\simeq$1 mm diameter); this introduces a significant error in the specimen-to-film distance and precludes very accurate results (Ref. 21). Also, we used a linear extrapolation, but more accurate methods are available.

In Fig. 8 all the low-gravity data points were adjusted downward by 0.9 pm in order to bring our value of a_o for iron into coincidence with the true one. The line drawn in Fig. 8 is taken from the work of Zwell, Carnahan, and Speich (Ref. 23), who have previously measured lattice parameters for these alloys solidified terrestrially. Both the low-gravity results and the terrestrial results display the same trend; low-gravity solidification does not seem to have altered this behavior.

D. External Morphologies

1. Overall Shape

A freely floating liquid droplet naturally assumes a spherical shape in order to minimize its surface energy. Under ideal conditions heat will be lost uniformly, and solidification will commence at the surface and proceed radially toward the center. Shrinkage due to solidification will appear as a spherical cavity in the middle of the specimen.

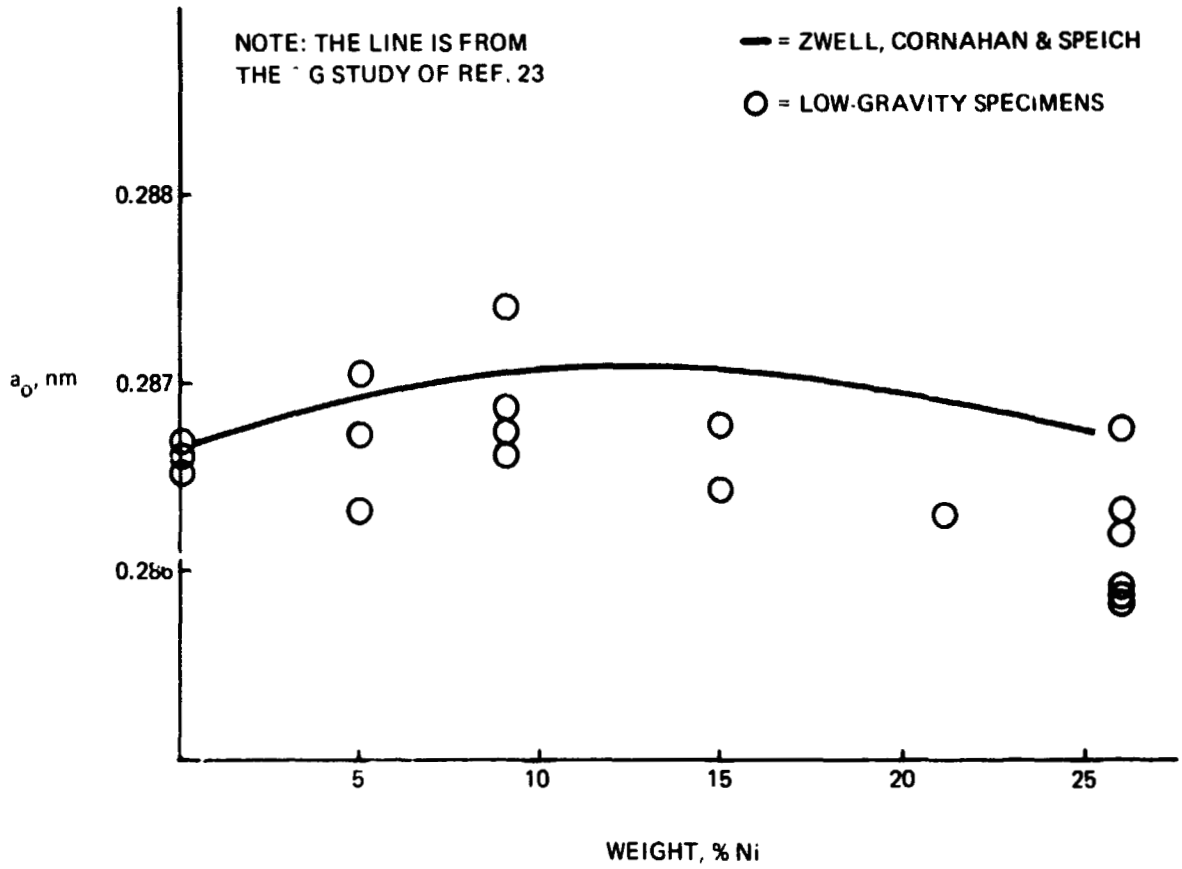

Fig. 8 Lattice Parameter of Fe-Ni Alloys Solidified in Low Gravity

We have obtained spherical specimens of both pure metals and alloys. Figures 9, 10, and 11 are scanning electron micrographs of spheres of pure iron, iron-9% nickel, and nickel-5% aluminum. However, not all of the specimens are perfect spheres; there are several reasons for this. Some specimens are released with a significant drift velocity and impact the specimen holder or chamber walls before they are solid; these specimens usually have obvious flat spots. Other specimens do not seem to have been completely molten or sufficiently fluid to achieve a spherical shape before solidifying.

Still others seem to have been spherical while liquid but their shapes have been perturbed by the solidification process. Solidification of the specimen shown in Fig. 12 seems to have begun near the bottom of the specimen and progressed upwards. The top remained sufficiently fluid to deform and eventually form a classic shrinkage pipe. This can be expected whenever solidification begins with nonspherical symmetry. The situation can be even more complicated, as illustrated by the specimen of W-25% Re shown in Fig. 13. The external shape is not spherical but is composed of a spherical cap, a conical section, and another spherical cap, with what appears to be some secondary or excess liquid flowed over the original surface near one joint. This bizarre shape is probably not accidental, since a large majority of our W-25% Re specimens displayed the same characteristics. It was initially hypothesized that this external shape was caused by banded peritectic solidification (Ref. 24, 25) and the different sections reflected different contact angles between the liquid and alpha and sigma phases. However, subsequent sectioning and metallographic examination revealed a uniform fine equiaxed microstructure of alpha tungsten with only very small amounts of sigma in the last region to solidify. Thus, we are unable to offer an explanation for the observed shape. It is implicit in the foregoing discussion (and obvious from the specimen shape) that solidification did not occur in a spherically symmetric manner.

The reason for this lengthy discussion is to emphasize the fact that a sphere is not necessarily the most probable shape for an uncontained droplet of metal solidified in the absence of gravity. In this experiment nonspherical shapes were observed in some cases because of solidification shrinkage and in other cases because of an unexplained but reproducible phenomenon, presumed to be related to the mechanism of solidification. Gas phase formation is another "intrinsic" reason for nonspherical shapes, as postulated to explain the results of the Skylab M553 experiment (Ref. 22). No evidence for such a gas phase formation was observed in this experiment, simply because the alloy systems investigated did not fulfill the criteria for operation of this mechanism (Ref. 22).

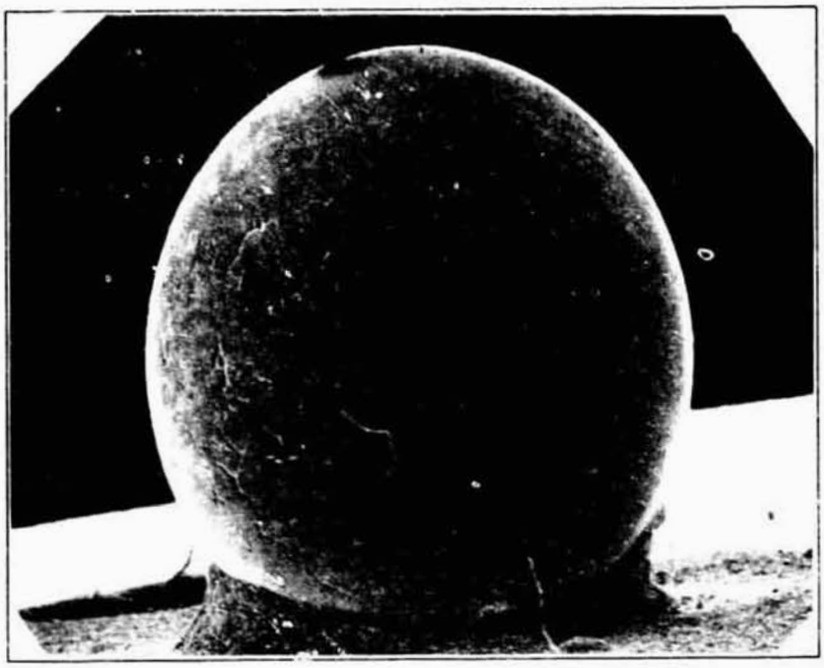

Fig. 9 SEM Micrograph of a Pure Iron Sphere, 70X

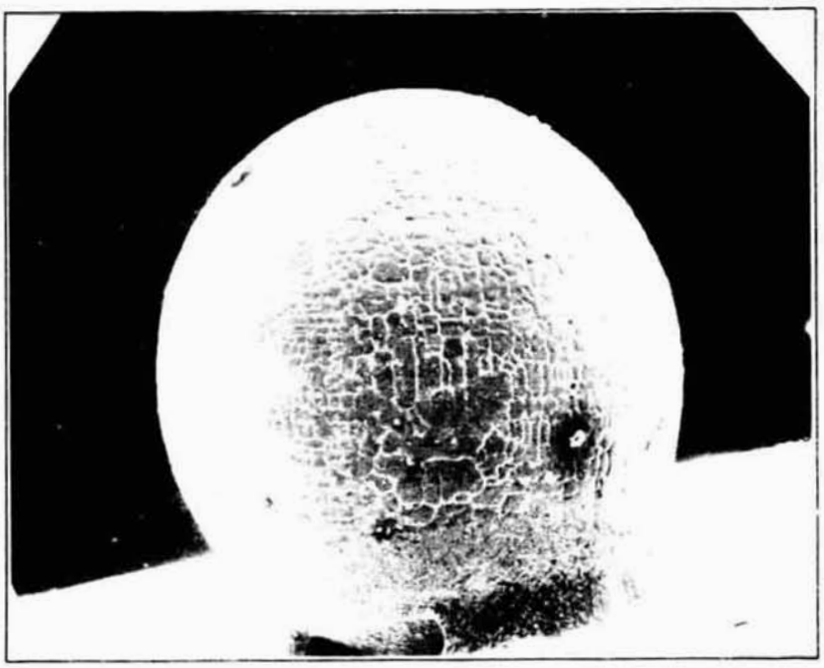

Fig. 10 SEM Micrograph of a Fe-9% Ni Sphere, 70X

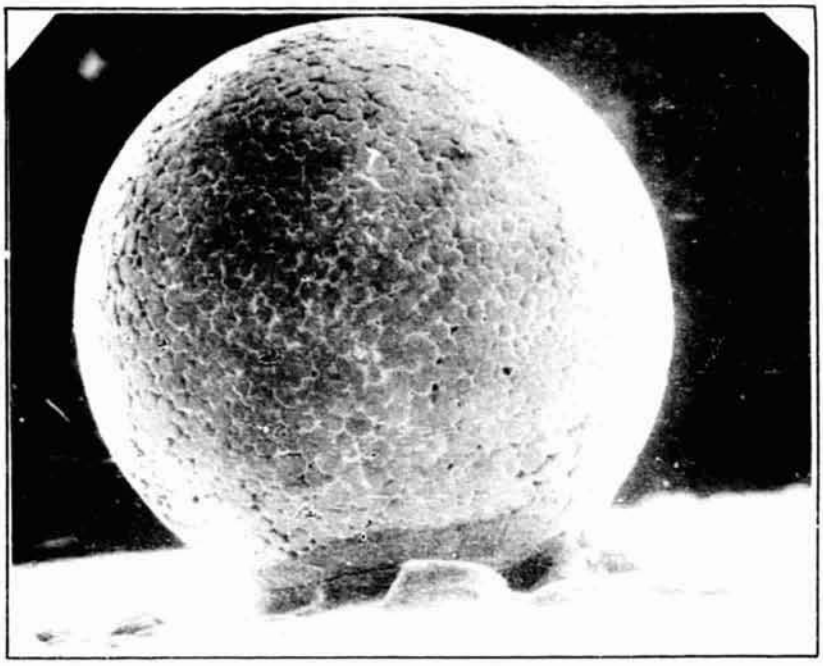

Fig. 11 SEM Micrograph of a Ni-5% Al Sphere, 65X

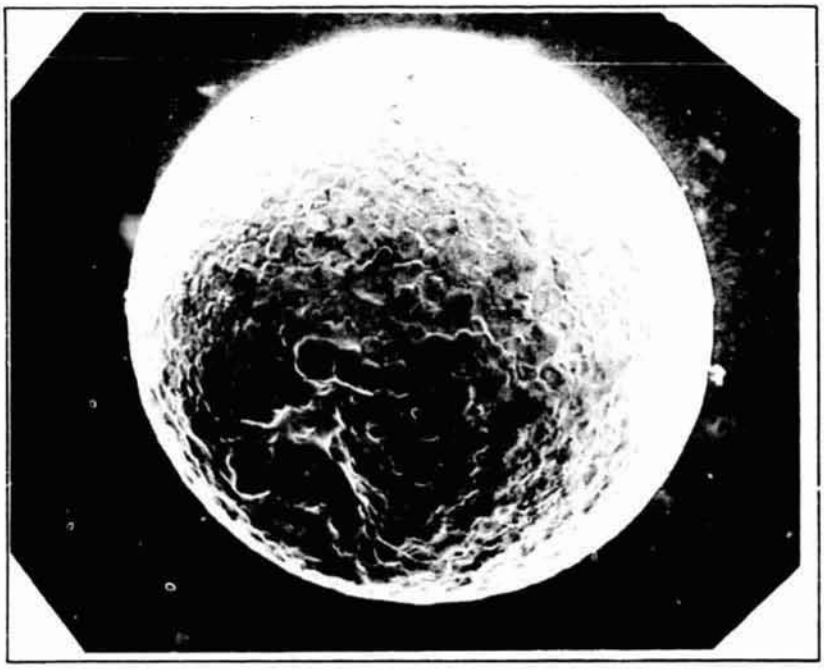

Fig. 12 SEM Micrograph of a Ni-5% Al Specimen with Pipe, 90X

Fig. 13 SEM Micrograph of an W-25% Re Specimen, 60X

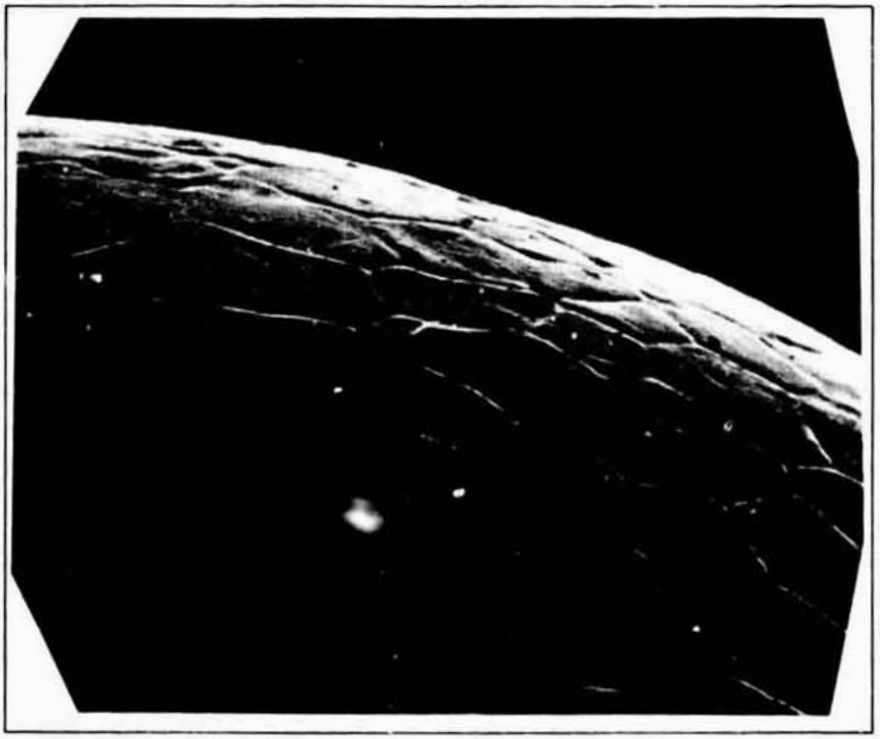

Fig. 14 SEM Micrograph of Surface of a Pure Iron Specimen, 650X

2. Surface Microstructures

A large variety of surface microstructures were observed and many of them are shown in the following scanning electron micrographs. Figure 14 shows the generally smooth, equiaxed grain structure of a pure iron specimen; similar structures were observed on a Fe-5% Ni sphere and on a sphere of pure silver. This is the simplest structure that could be anticipated, but it was not observed frequently. Figure 15 shows the surface of a Ni-5% Al specimen. The grain boundary grooves are deeper; in some cases voids are observed, as shown in Fig. 16. Pronounced grain boundary grooves (Fig. 15) are a typical feature of the Ni-5% Al specimens whereas voids appear infrequently. The pronounced grain boundary grooves are most likely due to solidification shrinkage but they could also have been caused by preferential evaporation of aluminum. The surfaces of the grains adjoining the void in Fig. 16 are extensively terraced in a crystallographic fashion. Similar terracing was also observed in the Skylab M553 experiment (Ref. 22). Terracing of this sort may be due to preferential evaporation from the solid surface during cooling after solidification, or it might be a last liquid effect, or it may be a record of growth steps which existed during the solidification process itself. Examination of Fig. 16 shows that the terraces exist on all the visible surfaces including those surfaces which were originally part of the spherical surface of the liquid drop. If this were a last liquid effect terracing would not be so widespread; it would be more localized as in the Skylab experiments (Ref. 22). Likewise, we would not expect to observe growth steps on lateral surfaces. Thus, we tentatively conclude that this terracing is due to crystallographically preferential evaporation after solidification.

The formation of steps during evaporation is a commonly observed phenomenon; Hirth and Pound (Ref. 26) review previous observations. It is generally thought that the formation of macroscopic steps is due to the presence of adsorbed impurities as proposed by Frank (see Ref. 26).

An obviously cellular/dendritic solidification morphology was observed in some of the iron-nickel specimens and a good example is shown in Fig. 10. A fully dendritic structure was observed on one of the steel specimens, Fig. 17. In general, dendritic surface structures were not observed; this is in contrast to the surface structures of atomized superalloys, Ref. 15. The surface structures of the Fe-Ni alloys were generally fine equiaxed grains with pronounced grain boundary grooves and an example is shown in Fig. 18. Closer examination of this surface reveals the existence of fine surface relief markings; these are shown in Fig. 19 and are presumed to be due to the martensitic transformation of γ to α . It is also noted that the prior austenite grain boundaries in Fig. 19 do not

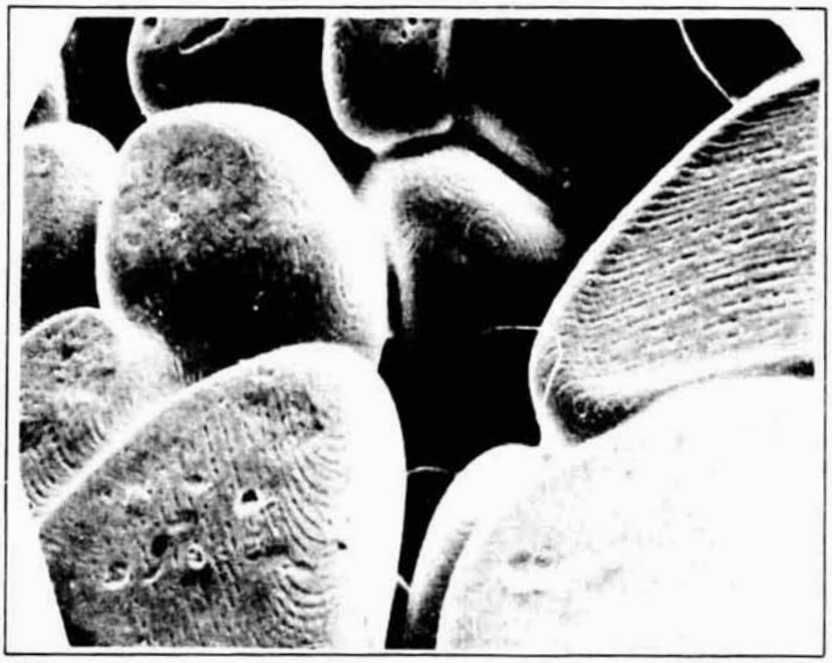

Fig. 15 SEM Micrograph of Surface of a Ni-5% Al Specimen, 900X

Fig. 16 SEM Micrograph of Terracing on a Specimen of Ni-5% Al, 1000X

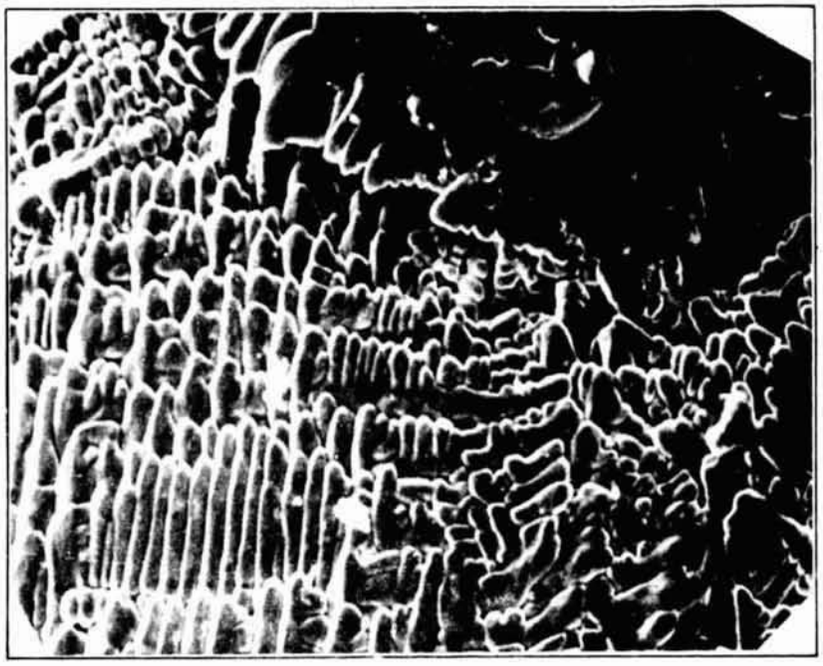

Fig. 17 SEM Micrograph of Dendrites in a 1090 Steel Specimen, 700X

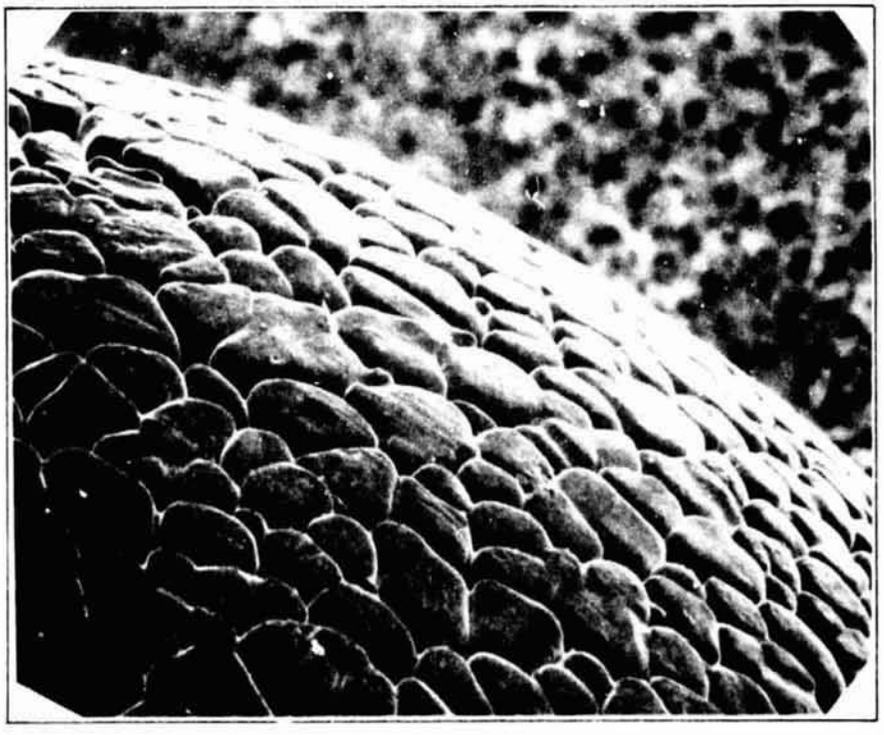

Fig. 18 SEM Micrograph of Surface of a Fe-15% Ni Specimen, 350X

coincide with the grain boundary grooves; this is due to grain growth. This observation is corroborated by the microstructures of etched cross-sections (refer to Section III, external morphologies). The lath-type martensitic surface relief of Fig. 19 (Fe-15% Ni) tended to become almost plate-like in the Fe-26% Ni alloy, as shown in Fig. 20. This is not unexpected, particularly if a small amount of carbon contamination was present (Ref. 27).

An unusual microstructure was observed on many of the iron-nickel alloys, as shown in Fig. 21 and 22. This microstructure consists of extensive terracing and blocky faceting, often with a central core or nucleus. The grain boundary grooves seem to contain a brittle phase that is cracked and sometimes separated from the neighboring grain. The terracing is often built up of layers of platelets. Some areas consist of blocky prisms or pyramids. Such microstructural features are atypical of metallic solidification. It is thought that these structures are caused by the presence of a significant partial pressure of oxygen in the test chamber during melting and solidification. These structures were present on most of the specimens of runs 13, 22, and 23, but were not observed on specimens of the same material in runs 34 and 36. The specimens from runs 13, 22, and 23 have a bluish surface color when examined with an optical microscope, whereas those from runs 34 and 36 are bright and shiny. Further, we were able to reproduce some of these structures by melting and solidifying small buttons of Fe-25% Ni in a bell jar at various partial pressures of oxygen. We were not successful in producing identical surface microstructures, but our limited success lends further credence to this explanation. The oxides of iron melt between 1420 and 1565°C and the melting points of the Fe-Ni alloys are between 1450 and 1520°C. Thus, it is quite possible that these microstructures are the result of low-gravity oxide solidification, and should not be thought of as typical of low-gravity metallic solidification.

Finally, an unusual and perplexing microstructure was observed on some of both the Fe-5% Ni, Fig. 23, and the 1090 steel specimens, Fig. 24. The surface consists of islands or buttes protruding in pronounced relief. On a macro-scale the tops of the buttes generate a spherical surface which has approximately the radius of curvature of the liquid sphere, but on a micro-scale the top of each butte is not necessarily convex. In fact, it is often concave. The spacing between buttes is variable: in the Fe-5% Ni specimens the spacing seems to correspond to the grain size, but in the 1090 steel sample not all of the grains protrude. Both samples show fine scale surface relief due to the martensitic transformation, although this is more apparent in the steel sample. Note that the prior austenite grain boundaries do not coincide with the valleys in the Fe-5% Ni specimen. Also note that both alloys are near their respective peritectic composition, 4.5% Ni for the Fe-Ni and 0.17% C for the Fe-C.

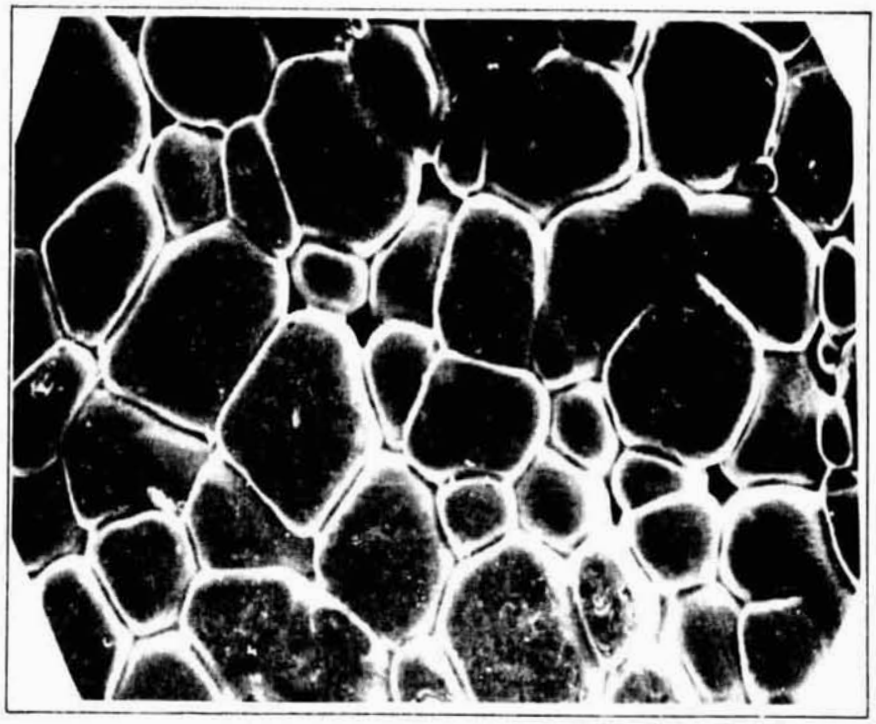

Fig. 19 SEM Micrograph of Surface of a Fe-15% Ni Specimen, 450X

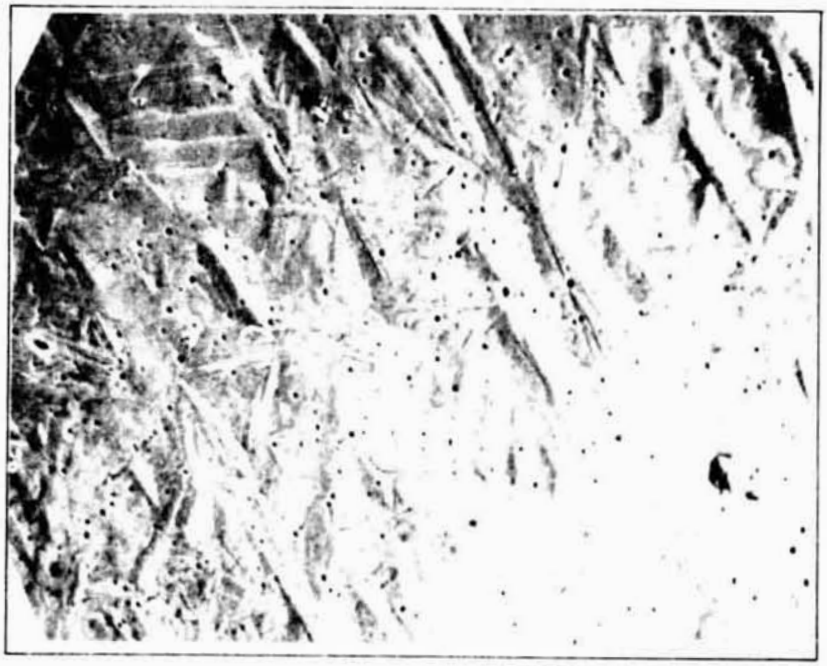

Fig. 20 SEM Micrograph of Surface of a Fe-26% Ni Specimen, 1500X

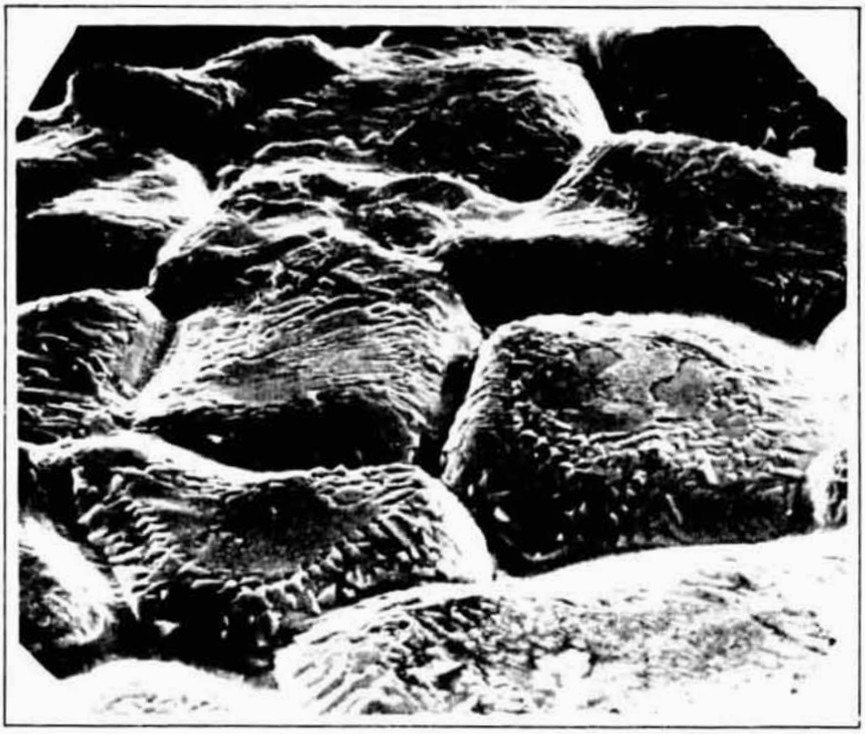

Fig. 21 SEM Micrograph of Surface of a Fe-26% Ni Specimen, 1700X

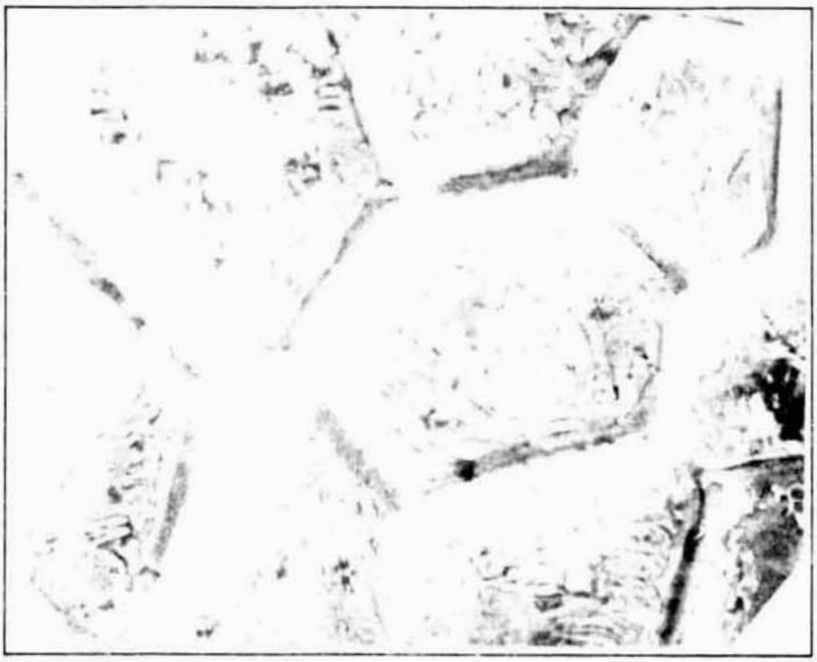

Fig. 22 SEM Micrograph of Surface of a Fe-25% Ni Specimen, 1500X

Fig. 23 SEM Micrograph of Surface of a Fe-5% Ni Specimen, 800X

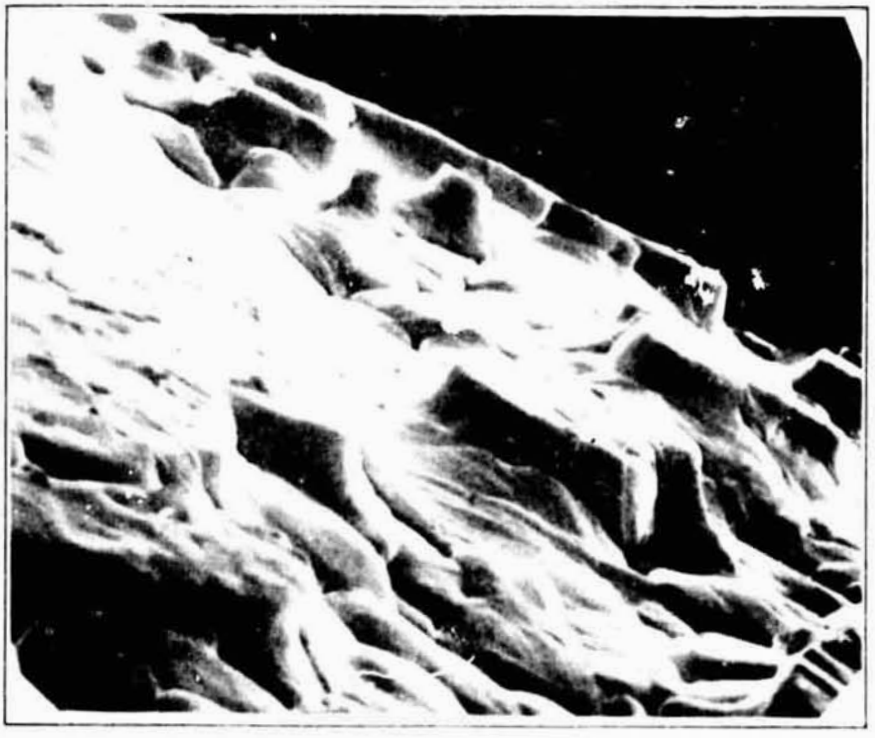

Fig. 24 SEM Micrograph of Surface of a 1090 Steel Specimen, 1400X

The nominal carbon content of the steel is 0.9 percent, but significant surface decarburization has occurred as will be discussed in the section on evaporative segregation.

Several suggestions have been offered to explain the origins of these structures. An immediate possibility is that the islands are remnant unmelted solid; this is discounted, however, because of the sharp perimeters of many of the islands. It is thought that partially melted regions would display well-rounded edges and should have cylindrical rather than spherical external surfaces.

It was suggested (Ref. 28) that the formation of small regions of solid on the liquid surface could perturb the heat flow and somehow give rise to these structures. This might occur due to a difference in emissivity or in thermal conductivity of the liquid and solid. The best available data (Ref. 20, 21) indicate that the total emissivity of iron does not change discontinuously at the melting point. Thus, the rate of heat loss due to radiation from the surface will not be perturbed by the formation of a solid and the surface should remain isothermal. The thermal conductivity of liquid iron is given as 0.403 watt $cm^{-1}.^{-1}$, that of solid iron 0.346, both at 1810 K (Ref. 20). The liquid is therefore a better conductor of heat and this may alter the process of solidification, but it is not apparent to the authors how this could give rise to a precipitous change of direction of the solidification front or to a concave surface.

A very significant difference exists, however, between the emissivity of a clean iron surface, approximately 0.3 an 1810 K, and that of iron oxide, approximately 0.8 at 1810 K (Ref. 20). If a small island of oxide formed on an otherwise clean liquid surface, the drastic increase in emissivity could lead to an immediate temperature drop and freezing of the underlying metal. The frozen island would propagate radially inwards and subsequent solidification could preserve its spatial location at the position of the original liquid surface. The remaining liquid would eventually solidify with concomitant feeding shrinkage, but a sharp boundary between the initially frozen islands and subsequently solidified material could be envisioned. In criticism of this mechanism, no obvious oxide film exists on these specimens.

An alternate mechanism for the formation of the islands hinges on the occurrence of undercooling. If the material were undercooled to a significant degree ($\simeq$150), rapid nucleation and solidification of the islands would result in an immediate recalescence due to the release of the latent heat of fusion. The temperature of the sample would rise close to the melting point, with solidification then proceeding at a slow rate. This would be accompanied by some partial remelting of the solid due to solute microsegregation and local superheating. Feeding of the solidification shrinkage would result in contraction of the material surrounding the islands, and might give rise to the observed structure.

Another suggestion is that this surface relief is a frozen-in record of Bénard cells. We can examine this hypothesis with a rough calculation. A convenient parameter for describing Bénard flow is the dimensionless wave number α , defined as $\alpha = (2\pi d/\lambda)$ where d is the film thickness and λ is the intercellular spacing. For typical Bénard flows $\alpha = 2$ (Ref. 29). Taking $\lambda = 25$ μm, from Fig. 23 we calculate a film thickness d of approximately 10 μm. We now substitute this value of d in the expression for the Marangoni number, M:

$$M = \frac{(d\gamma/dT)d\Delta T\rho C_p}{\mu K}$$

where

γ = surface tension
ΔT = temperature difference across the film
μ = viscosity
K = thermal conductivity
C_p = specific heat

Taking K = 0.403 watt/cm K (Ref. 20), $\mu = 5\text{x}10^{-2}$ P (Ref. 20), $C_p = 0.15$ cal/gm K (Ref. 24), and $(d\gamma/dT) = 0.5$ dyne/cm K (Ref. 30). Using M = 80 as a critical value for cell formation (Ref. 31) we obtain $\Delta T \simeq 700$ K. It is unlikely that a 10 μm thick film of liquid metal could support a temperature difference of this magnitude so, on the basis of the calculation, it seems unlikely that Bénard cells could exist on the surface of the liquid sphere. However, it has been shown that $d\gamma/dT$ is very sensitive to impurities and can vary from 0.5 to 3.0 dyne/cm K (Ref. 32). Thus we cannot rule out some localized impurity related effect.

A final suggestion (Ref. 33) is that these are frozen-in records of upwellings caused by convection from a hot core to the cooler surface, similar to the upwellings observed in stars such as the sun. This suggestion was not pursued in detail because of the short experimental times involved and the absence of any source of heat in our specimens.

E. Cross-Sectional Microstructures

Optical metallography of polished and etched cross-sections provided information on the distribution of shrinkage porosity, grain size, and post-solidification transformations.

When spherical specimens were sectioned the distribution of shrinkage porosity was found to be variable. In some specimens the voids were distributed homogeneously throughout the section; in others the porosity tended to be more localized. Figure 25 shows localized porosity in a sphere of Fe-26% Ni. The porosity in this specimen tends to be concentrated near the center, but a significant amount also exists nearer the surface. In general, the porosity was more homogeneously distributed than that of Fig. 25, indicative of homogeneously distributed nucleation and growth as opposed to surface nucleation and radial growth.

All the specimens examined were found to have a fine-grained equiaxed structure. Figure 26 is a micrograph of a Ni-5% Al specimen etched for 30 s in 1:1 $HN0_3$:HAC. The mean linear intercept grain size, $\bar{\ell}$, is approximately 13 μm. Identical microstructures were observed in the other Ni-5% Al specimens although the grain size varied with specimen diameter as shown in Table 3.

A fine-grained equiaxed structure was also observed in the Fe-Ni specimens. Figure 27 is a specimen of Fe-26% Ni etched with 5 percent picral for 8 minutes. The grain boundaries appear as indistinct areas unlike the usually observed sharp delineation. Further etching with nital revealed another set of grain boundaries, as shown in Fig. 28. These boundaries etch in a more distinct manner; they almost coincide with the original set near the perimeter of the specimen but not near the center. An additional feature of the microstructure visible in Fig. 28 is the martensitic nature of the entire specimen. This is more easily seen in the magnified view shown in Fig. 29. When etched in nital the entire specimen was seen to be lath-type martensite, as is typical for these alloys (Ref. 27).

This compound microstructure can be explained in a straightforward manner. The fine equiaxed grain structure, Fig. 27, is thought to be a record of the structure immediately after solidification; thus the differential etching is due to variations in nickel concentration caused by solute partition and rejection during solidification. This idea is confirmed by microprobe analysis (refer to the section on cross-sectional microstructures). Immediately after solidification; while cooling through the austenite field, sufficient time was available for grain growth to occur in the center of the specimen. Grain growth did not occur at the surface because of the more rapid cooling. Thus the distinct grain boundaries, Fig. 28, are the prior austenite boundaries after grain growth. Subsequently, the austenite transformed to martensite upon cooling below M_s. To confirm this explanation, the martensite colonies are observed to traverse the indistinct grain boundaries easily but change direction at the distinct, prior austenite boundaries.

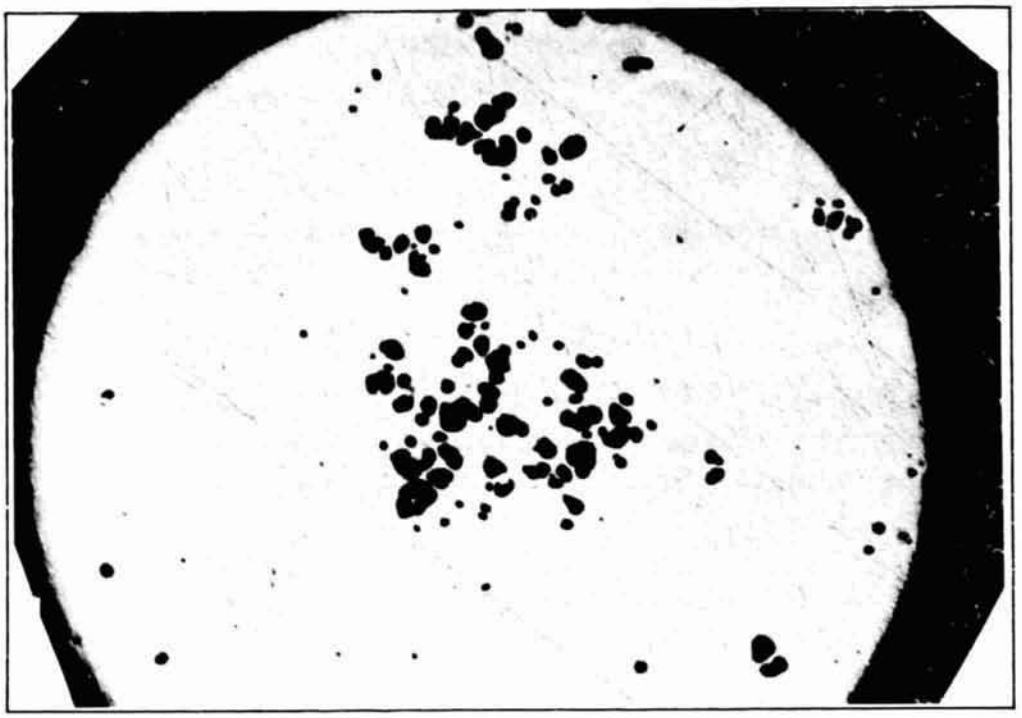

Fig. 25 Optical Micrograph of an Unpolished Section of a Fe-26% Ni Specimen, 72X

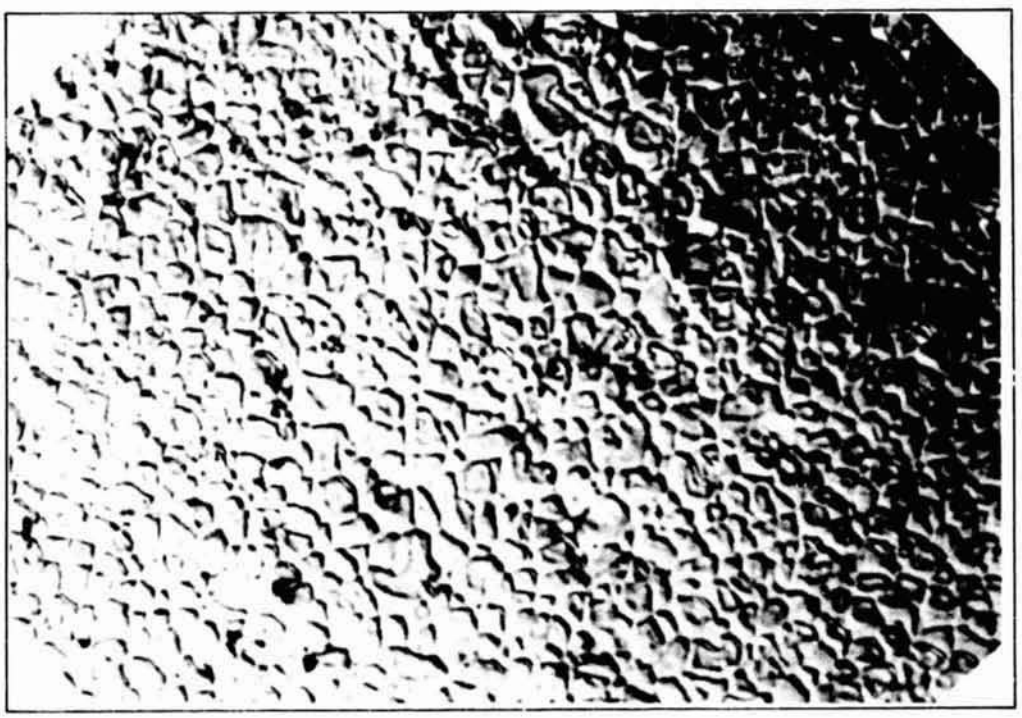

Fig. 26 Optical Micrograph of an Etched Cross-Section of an Ni-5% Al Specimen, Nomorski Contrast, 220X

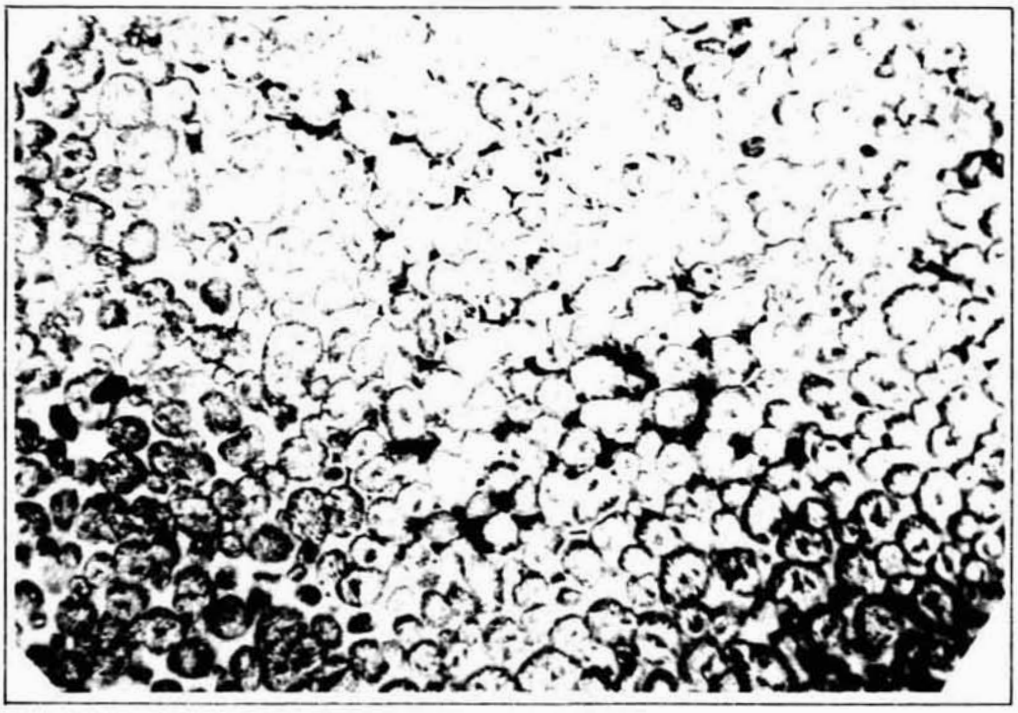

Fig. 27 Optical Micrograph of an Etched Cross-Section of a Fe-26% Ni Specimen, Picral, 145X

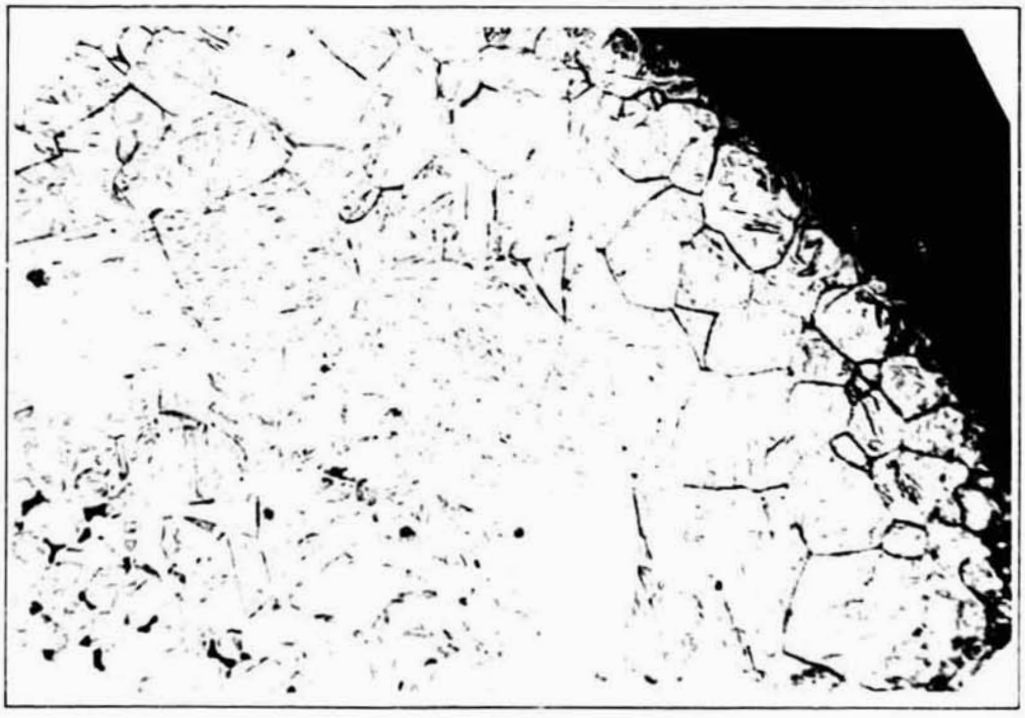

Fig. 28 Same Specimen as Fig. 27 with Additional Etching in Nital, I45X

Fig. 29 Same Specimen as in Fig. 28, Repolished and Etched With Marbles Reagent, 400X

Specimen diameter influenced the observed grain size and the extent of grain growth. Table 3 gives values for the mean linear intercept grain size of the original grain structure, the maximum prior austenite grain size at the center of the specimen ℓ_γ, and the external diameter of the specimen, d. Note that the larger, more slowly cooled specimens exhibit correspondingly greater initial grain size and prior austenite grain size. The sting-mounted specimens have the smallest grain sizes and do not show any evidence of grain growth. This grain size variation is directly related to the local solidification time and, hence, cooling rate.

It has previously been observed (Ref. 34) in Fe-25% Ni that the dendrite element spacing, $\bar{\ell}$ (μm), is related to the local solidification time according to the relation

$$\bar{\ell} = 38\ t_s^{\ 0.45} \tag{11}$$

The dendrite element spacing is defined as the secondary dendrite arm spacing in dendritic microstructures or the mean linear intercept grain size in equiaxed microstructures. This relation was found to be valid independent of the degree of undercooling, but the grain morphology changed from dendritic to equiaxed for undercoolings greater than 170K. Applying Eq 11 to the data of Table 3, we can calculate the expected grain size. These figures are shown in column 7 of Table 3 and agree reasonably well with the observed values given in column 4; thus, we conclude that the relationship is valid for our experiment. We note that our specimens always displayed fine equiaxed microstructures, indicative of undercoolings greater than 170 K. This will be discussed further in Section IV.

Retained austenite was not observed metallographically or by X-rays in any of the Fe-Ni specimens. Thus they are assumed to be fully transformed.

F. Solute Redistribution

The redistribution of solute was studied in some of the alloy materials; the two objectives of these measurements were to a) determine the extent of evaporative segregation, and b) to study the effect of low-gravity solidification on localized solute redistribution. These two phenomena will be addressed in turn.

1. Evaporative Segregation, Predictions

It is instructive to estimate the amount of material loss due to evaporation that might be expected in our experiment. We first calculate the approximate evaporation rates for the pure components at the liquidus temperature of the alloy in question using Eq. 10.9 and data from Table 10.2 of Ref. 18. The evaporation rates, W_o (gm cm^{-2} s^{-1}), calculated

TABLE 3. GRAIN SIZES OF VARIOUS SPECIMENS

Material	Specimen	d (mm)	ℓ (μm)	$\ell_{\gamma' max}$ (μm)	t_s (s)	ℓ_{calc} (μm)
Ni - 5% Al	1-B	0.8	30			
Ni - 5% Al	2-1A	0.7 †	13			
Ni - 5% Al	3-1P	0.9 †	13			
Fe - 15% Ni	23A	1.8	32	150	1.1 *	40
Fe - 26% Ni	22A	1.7	33	150	10 *	38
Fe - 26% Ni	22K	0.8	20	27	0.48 *	27
Fe - 26% Ni	22J	0.9 †	13	13	0.12	15

† Attached to sting

* Calculated from Eq 9

TABLE 4. EVAPORATION CHARACTERISTICS OF MATERIALS STUDIED

Material	T(k)	W_o (gm $cm^{-2}s^{-1}$)	x_i	a_i	W_i (gm $cm^{-2}s^{-1}$)
Al	1700	2×10^{-3}	0.1	0.1	2×10^{-4}
Ni	1700	3×10^{-5}	0.9	0.9	3×10^{-5}
Ni	1725	4×10^{-5}	0.25	0.17 *	7×10^{-6}
Fe	1725	7×10^{-5}	0.75	0.74 *	5×10^{-5}
C	1750	4×10^{-13}	0.041	0.032 *	1.3×10^{-14}
Fe	1750	1×10^{-4}	0.959	0.954 *	3×10^{-4}

* For T = 1873 K

in this manner are listed in column three of Table 4. For evaporation from alloys, these figures must be modified. The evaporation rate, W_i, of component i in an alloy is given by

$$W_i = a_i W_o \tag{12}$$

where a_i is the activity of component i (Ref. 18). When activity data are not available, it is customary to assume Raoult's law (Ref. 18) which is

$$a_i = x_i \tag{13}$$

where x_i is the atom fraction of component i in the alloy. We were able to find activity data at 1813 K for the Fe-25% Ni and Fe-0.9% C alloys (Ref. 13); these values are shown in column 5 of Table 4 and the calculated values of W_i are given in column 6. The temperature of the activity data is slightly higher than the temperature in question, but this error is thought to be negligible. Activity data for Ni-5% Al in the liquid state were not available; thus Raoult's law was assumed. It should be noted, however, that the activity of aluminum in Ni-5% Al alloys displays very strong negative deviations from Raoult's law at lower temperatures. Hultgren, et. al. (Ref. 30), give $a_{Al} = 3 \times 10^{-6}$ for $x_{Al} = 0.1$ at 1273 K. It is unwise to extrapolate this behavior to 1700 K but we should bear in mind the possibility that the vapor pressure of aluminum in the Ni-5% Al alloy may be much lower than the figure given in Table 4.

With values of W_i calculated, we can estimate the total amount of material that could be lost during the experiment. We ignore evaporative losses before and after solidification and consider only the interval during which solidification actually occurs. Omission of the superheating interval is unfortunate, but it is impossible to estimate the superheat temperature; we justify this neglect because the superheat times are short (< 0.01 s). We also ignore any loss of the more slowly evaporating species. Thus, for the total weight of material lost, M, we have

$$M_i = W_i A t \tag{14}$$

where A = surface area and t = time interval.

For a typical specimen d = 0.1 cm, $A = 3.14 \times 10^{-2}$ cm^2 and t = 0.5 s (see Table 2). Thus for Ni-5% Al

$$M_{Al} = 3 \times 10^{-6} \text{ gm}$$

for Fe-25% Ni

$$M_{Fe} = 8 \times 10^{-7} \text{ gm}$$

and for Fe-0.9% C

$$M_{Fe} = 5 \times 10^{-6} \text{ gm}$$

These amounts represent a loss of 1.5, 0.03, and 0.1 percent of the total amount of the component present in the respective alloys. If these losses were distributed homogeneously throughout the sample (i.e., infinite solid state diffusivity) they would be undetectable. The losses should, however, be localized at the surface. Assuming no redistribution occurred, the depth to which all of the evaporating species would be removed is 2.5 μm in the Ni-5% Al, 0.04 μm in the Fe-25% Ni, and 0.2 μm in the Fe-0.9% C. These depths are rather shallow; the microprobe cannot resolve concentration differences on this scale (see below). However, we would expect some redistribution of solute to occur. This can be estimated as $\bar{x} = \sqrt{Dt}$, where $\bar{x}$ is a characteristic distance over which diffusion could occur. Using the typical (one gravity) liquid diffusion coefficient of $D = 10^{-5} cm^2 s^{-1}$ (Ref. 35) with t = 0.5 s, we have $\bar{x} = 22 \mu m$. Composition variation may occur to approximately $2\bar{x}$.

In summary, we see that for our experimental conditions we might expect some material loss due to evaporation. In the Ni-5% Al alloy preferential evaporation of aluminum should occur; in the Fe-25% Ni and Fe-0.9% C iron will be preferentially evaporated. The total amount of material lost should be undetectable for the Fe-25% Ni and Fe-0.9% C, but possibly observable in the Ni-5% Al. If observed, the loss of aluminum should be confined to the outer 40 μm of the specimen. These conclusions are of a tentavie nature; the evaporation process could be perturbed by a great many factors such as the formation of a surface oxide. A more complete discussion of the possibilities will be found in Ref. 14.

2. Evaporative Segregation, Observations

We observed the depletion of carbon near the surface of the 1090 steel specimen. This depletion extended to a depth of approximately 50 μm and was detected by a change from the normal martensitic/pearlitic microstructure to a ferritic one (Ref. 5). This behavior is opposite to the predictions of evaporation theory. However, decarburization of iron is not unusual; it is in fact the foundation of steelmaking. The presence of small amounts of oxygen, carbon monoxide, or hydrogen in the atmosphere would account for the observed decarburization. Oxygen is thought to be the likely culprit. We can estimate the amount of decarburization to be expected in our experiment from the data of Baker, et, al. (Ref. 36). During decarburization of levitated iron droplets, they found the rate of decarburization to be 7×10^{-5} gm cm^{-2} s^{-1} in a partial pressure of 0.01 atm of oxygen at 1900 K. For our 0.1 cm diameter sphere and 0.5 s, this gives a total carbon loss of 11×10^{7} gm or 3 percent of the total carbon present at the start. This represents all the carbon present in the outer

spherical shell (5 μm thick). Extensive carbon rearrangement is expected, however, since D_C (1750 K) >> 10^{-5} cm^2 s^{-1}, even in solid iron, Ref. 37, so we see that the observed decarburization and carbon redistribution can be easily explained. Thus, we conclude that it is likely that a small residual partial pressure of oxygen in our static vacuum was responsible for the observed decarburization and that the effects of evaporation were negligible in comparison to this reaction.

The electron microprobe was used to characterize the near surface solute distribution in the Fe-26% Ni and Ni-5% Al. Four traverses made on polished cross-sections of Fe-26% Ni samples are shown in Fig. 30, 31, 32, and 33. Each traverse began at the edge of the sample and proceeded inwards in 3.1 μm steps. The data points at 0 and 3.1 μm are not valid because the observed total count rates were far below the total count rates for the 6.2 μm and subsequent measurements. Thus, the volume of the sample excited in the 0 and 3.1 μm measurements was less than normal. Since the volume of the sample giving rise to the nickel X-rays is not necessarily the same as the volume giving rise to the iron X-rays, these measurements are unacceptable. Further, the quantitative X-ray resolution given by Reed and discussed in Ref. 38 is 6.6 μm for Ni in Fe. Thus, we report only the 6.2 μm and subsequent measurements.

Figure 30 is a traverse taken on a cross-section of the original, unmelted specimen wire. It shows an average composition of 23.1 percent nickel with a maximum segregation ratio, S, of 1.05. The segregation ratio is defined as the ratio of the nickel concentration in a grain boundary to the nickel concentration in the grain center. For our immediate purposes we report as S the ratio of adjacent maxima and minima as seen on the microprobe traverse.

Figures 31, 32, and 33 are traverses from three Fe-26% Ni samples solidified in low gravity. In each case there are pronounced peaks and valleys in the nickel concentration as a function of distance. Subsequent etching and examination shows that the peaks occur when cell boundaries are intersected by the probe trace. In confirmation, the mean interpeak distance, $\bar{p}$, is observed to be equal to the mean linear intercept grain size $\bar{\ell}$ as shown in Table 5. Maximum segregation ratios are given in Table 5. In all cases, S_{max} for the low-g melted samples is significantly greater than S_{max} for the unmelted sample. The presence of this pronounced grain boundary nickel segregation effectively masks any possible near-surface observations on evaporative segregation, as we are unable to separate grain boundary effects caused by redistribution during solidification from evaporation effects. Both processes take place on the same scale (spatially) in this experiment. This limitation

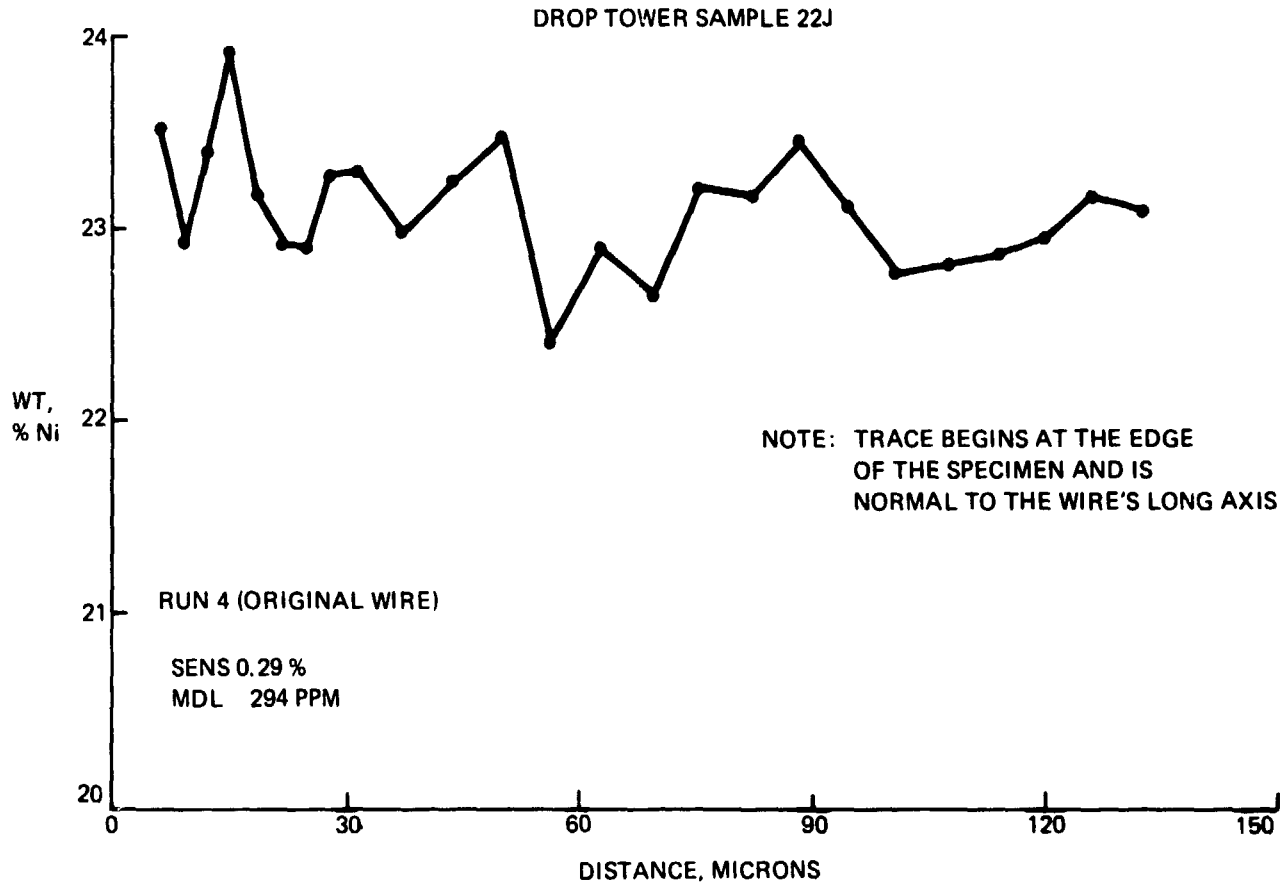

Fig. 30 Microprobe of Nickel Content in a Longitudinal Cross-Section as Drawn Fe-26% Ni

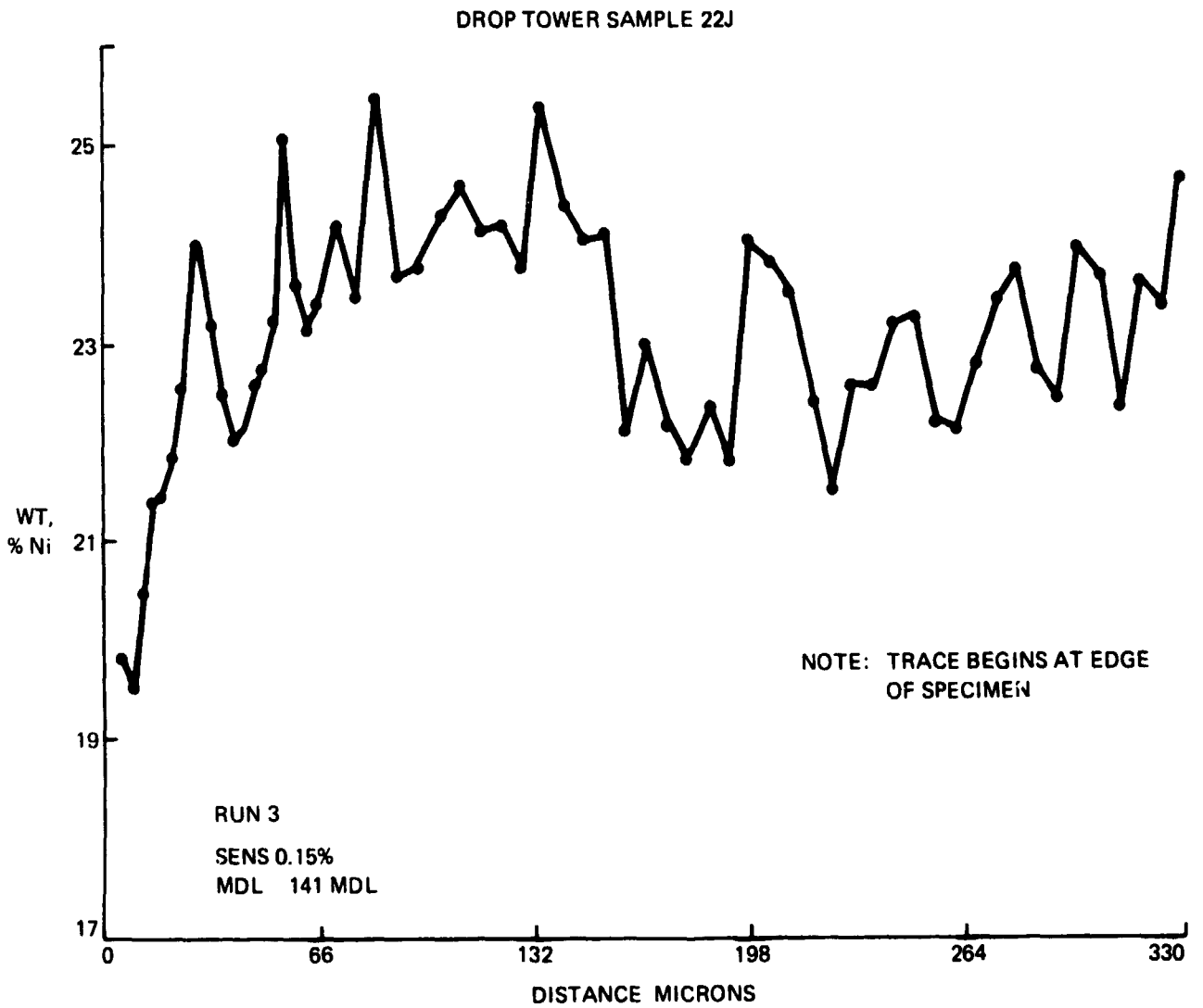

Fig. 31 Microprobe Trace Taken on a Cross-Section of Specimen 22J (Fe-26% Ni)

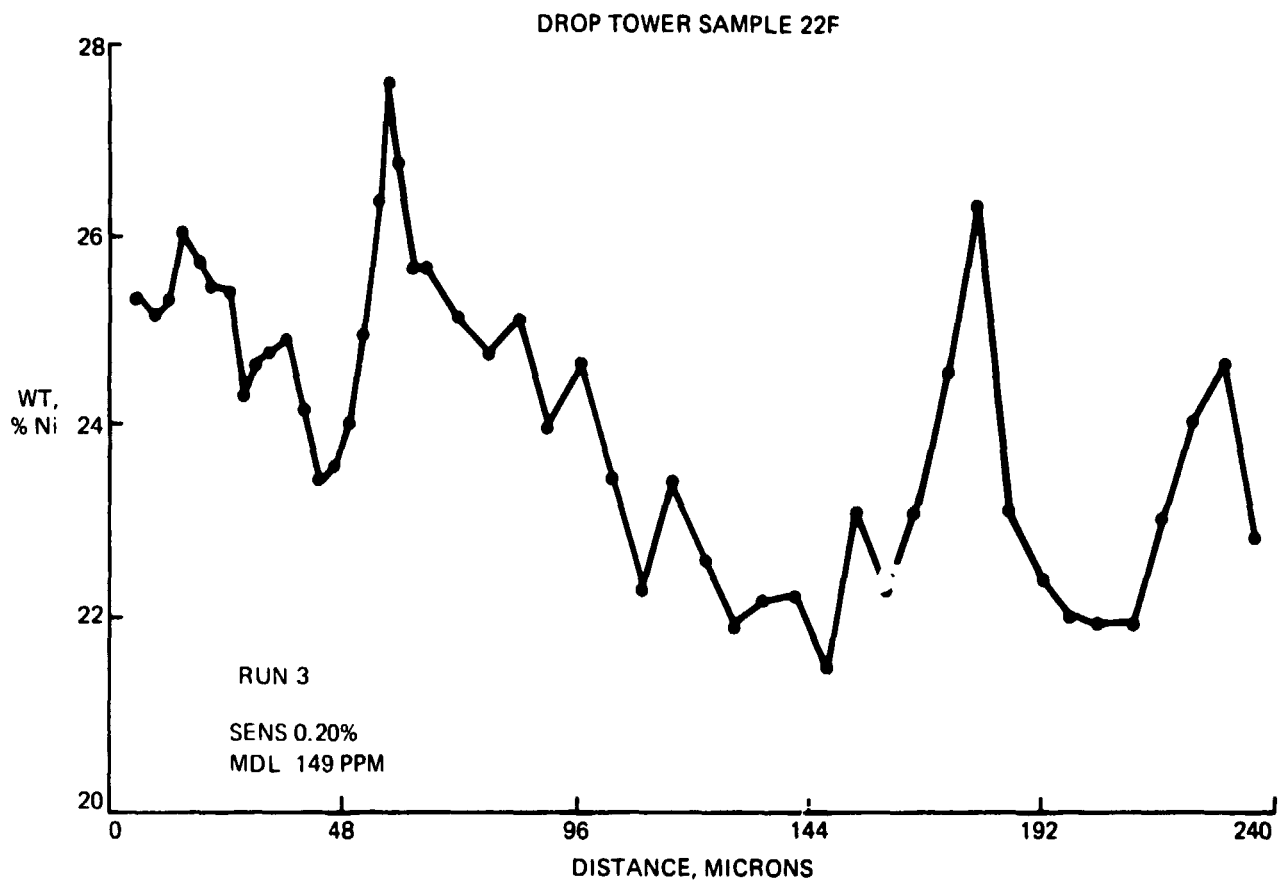

Fig. 32 Microprobe Trace From Specimen 22F, Same Conditions as Fig. 31

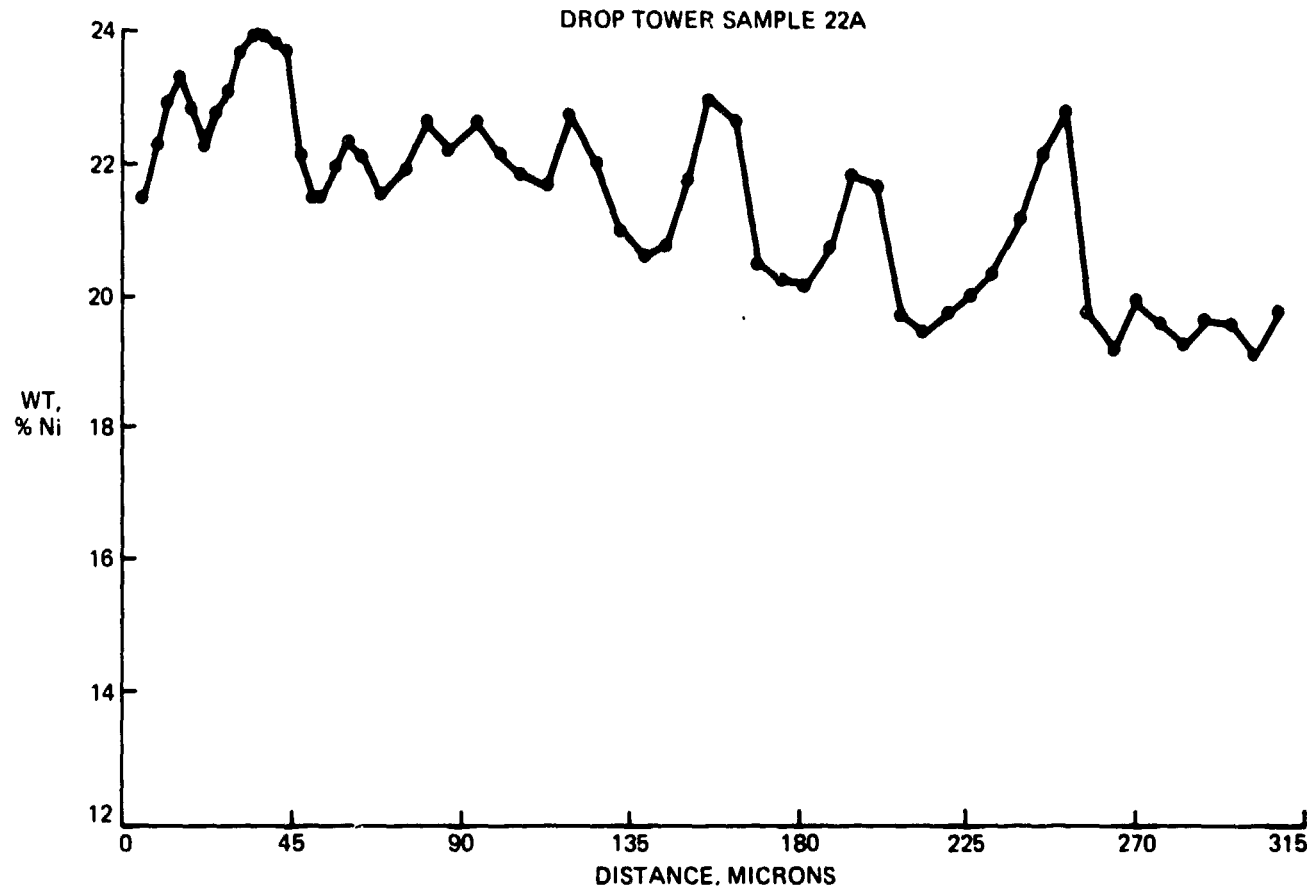

Fig. 33 Microprobe Trace From Specimen 22A, Same Conditions as Fig. 31

TABLE 5. OBSERVED SEGREGATION RATIOS

Material	Sample	d (mm)	S_{max}	$\bar{p}$ (mm)	ΔT
Fe - 26% Ni	22A	1.7	1.19	29	70
Fe - 26% Ni	22F	0.8	1.20	24	50
Fe - 26% Ni	22J †	0.9	1.15	27	135
Fe - 26% Ni	22J	‡	1.05		
Ni - 5% Al	2-1A	0.8	1.4	17	
Ni - 5% Al	3-1P	1.0	1.35	17	

† Sting mounted

‡ Unmelted wire

might have been circumvented if nucleation had occurred only at the surface, but that was not the case for these specimens (refer to Section III on X-ray studies and external morphologies).

If the peak-to-valley concentrations are smoothed out and ignored, Fig. 31 shows a general drop in the nickel content in the last 100 μm as the surface is approached. Figure 32 shows a possible increase and Fig. 33 shows a fairly level approach on the same scale. From our estimates in Section III (cross-sectional microstructures) we see that redistribution due to surface evaporative losses and subsequent diffusion over a distance of 100 μm is highly unlikely (i.e., for $D = 10^{-5}$ cm^2 s^{-1} and $\bar{x} = 100$ μm, $t = 10$ s). In any event, no consistent trend is observed. To summarize, we are unable to detect any effect of evaporative segregation in the Fe-26% Ni specimens.

Electron microprobe traces from two Ni-5% Al specimens are shown in Fig. 34 and 35. These traces are qualitatively similar to the Fe-26% Ni traces; they show pronounced peaks at grain boundaries and valleys at grain centers. Maximum segregation ratios and mean interpeak spacings are given in Table 5. We do not give data points at 0 and 3.1 μm for the same reasons as in the Fe-26% Ni traces. The calculated quantitative X-ray resolution for Al in Ni is also 6.6 μm, Ref. 38.

There is some indication of a reduction in the aluminum concentration as the surface is approached. Unfortunately, the amount of reduction is of the same order of magnitude as the grain boundary segregation. It is thought, however, that this may be a genuine evaporative segregation effect, but we are unable to draw a definite conclusion, particularly in view of the uncertainty in the aluminum evaporation rate.

3. Localized Solute Redistribution

The microprobe traces in Fig. 31 through 35 show extensive solute segregation on the same scale as the grain size in the Fe-Ni alloys. We investigated this redistribution by making additional microprobe traces. Microhardness indentations were made in areas of interest on the etched cross-section. The sample was then repolished to remove topographic effects of the etch, microprobe data were taken, and the exact location of the trace was established by photographing the carbon contamination spots left by the electron beam. Superposition of the negatives of the trace and the etched structure gave the precise location of the trace. A typical result is shown in Fig. 36. There is an exact correspondence between location of the peak nickel compositions and the grain boundaries. Likewise, the minimum nickel concentrations were found at the grain centers. Repetition of this type measurement on specimens 22A, 22F, and 22J (all Fe-26% Ni) and specimen 3-1P (Ni-5% Al) give the same

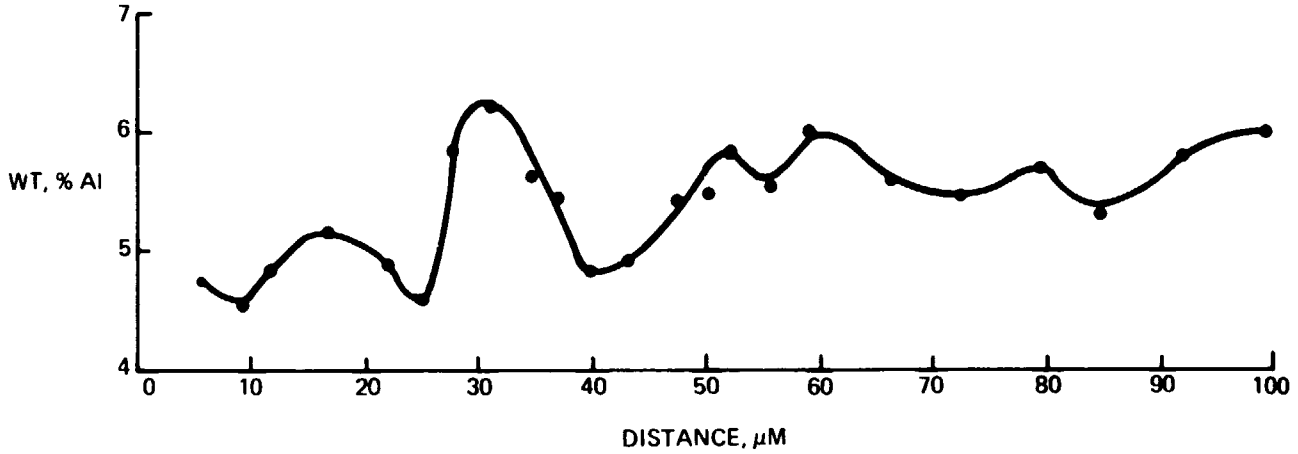

Fig. 34 Microprobe Trace From Specimen 2-1A (Ni-5% Al), Same Conditions as Fig. 31

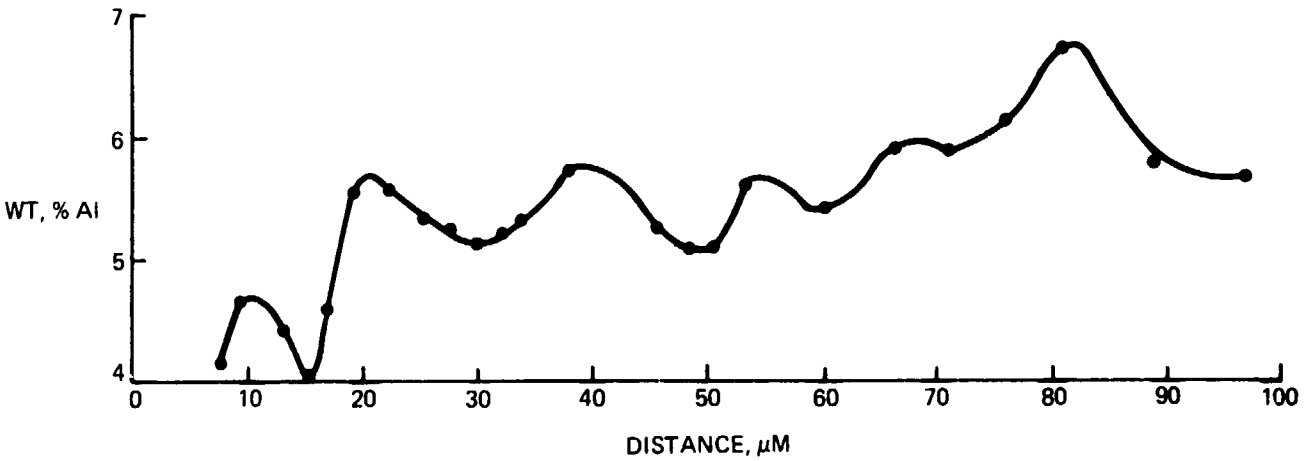

Fig. 35 Microprobe Trace From Specimen 3-1P (Ni-5% Al), Same Conditions as Fig. 31

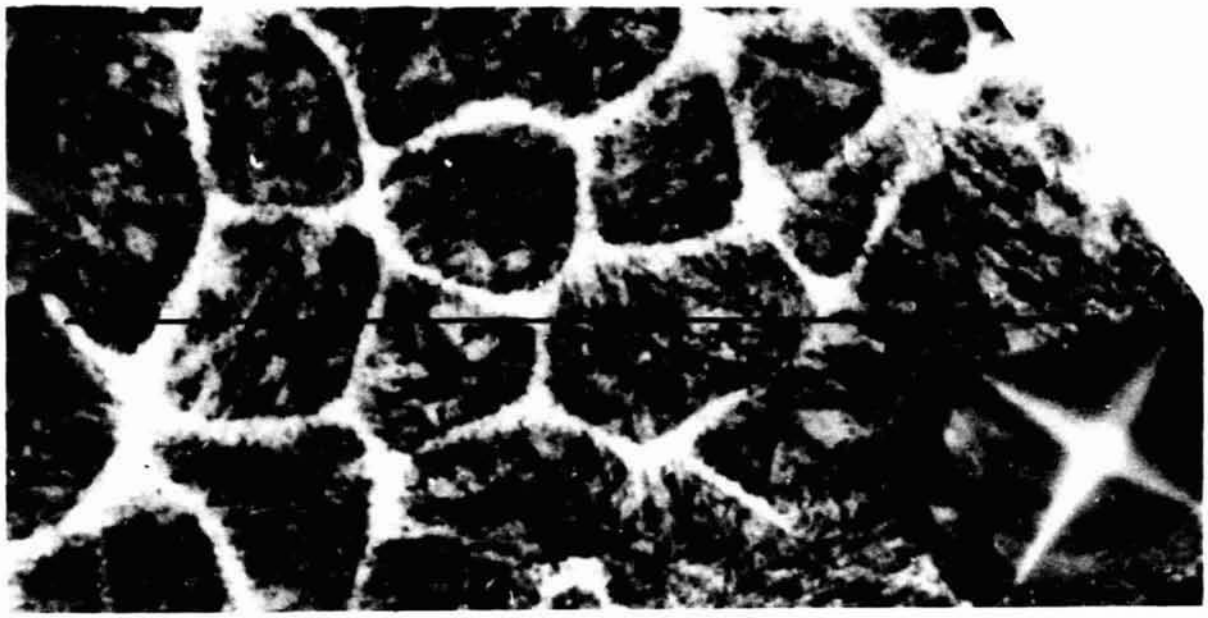

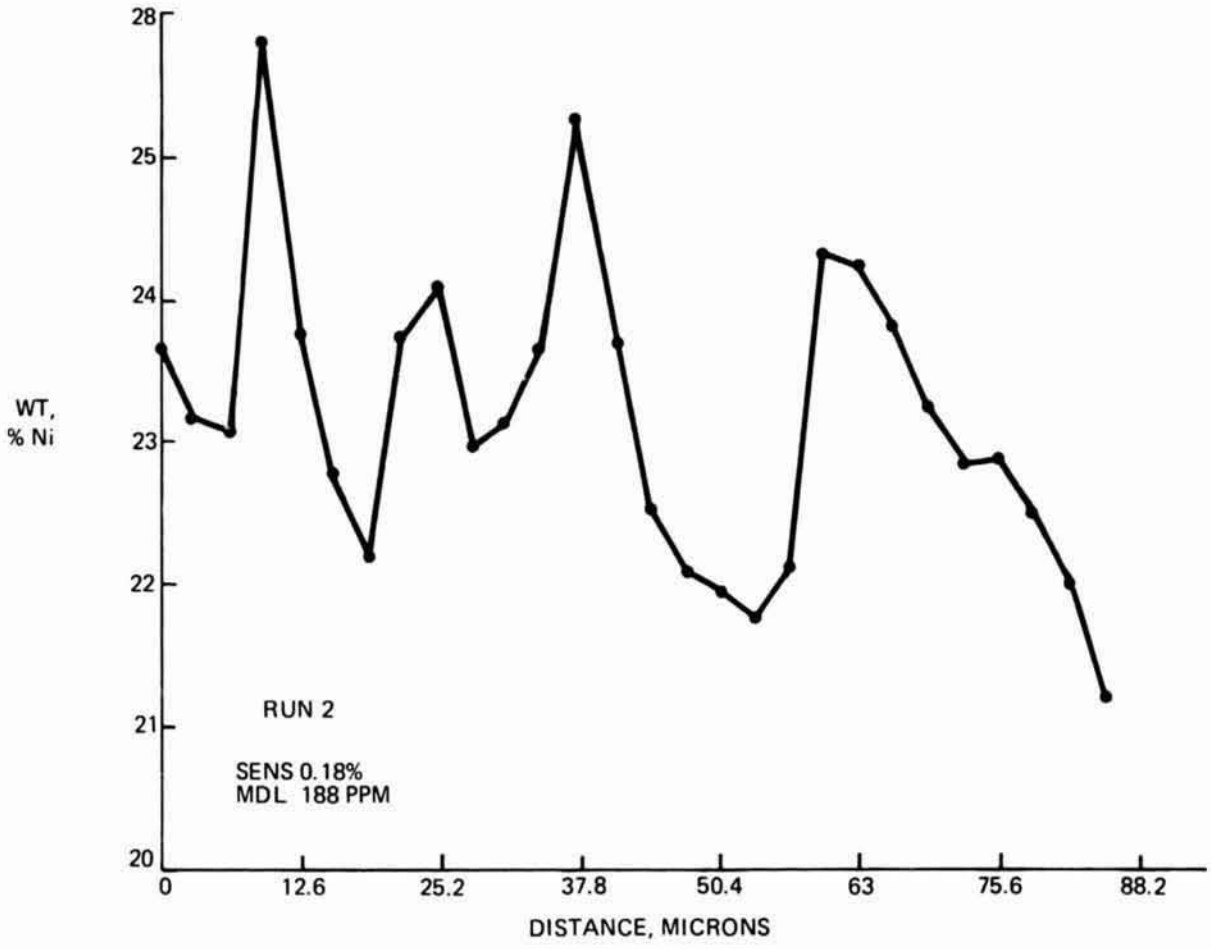

Fig. 36 Microprobe Trace From Specimen 22J and Associated Microstructure

result. In all of the Fe-26% Ni specimens, the peaks were found to correspond to the sometimes indistinct, light etching grain boundaries as in Fig. 27 and 36. No peaks in nickel concentration were found when traversing prior austenite grain boundaries. These observations confirm the identity of the light etching areas as the original solidification substructure and confirm the supposition that the peaks in the original microprobe traces are due to grain boundary segregation. This nickel segregation could only have occurred during solidification. Note that the microprobe traces show no evidence of high solute content dendrite cores which would be indicative of undercooling, Ref. 39.

The amount of nickel segregation is a function of the solidification process. Table 5 lists the maximum observed values of the segregation ratio, S. The maximum value is taken as characteristic of the solute redistribution because, in most cases, the probe trace does not pass directly through the grain center and thus does not measure the true value of S. Previous work on solute redistribution during solidification of Fe-25% Ni has shown that the segregation ratio in undercooled ingots is a function of the amount of undercooling (Ref. 40). It was observed that the segregation ratio decreased linearly with undercooling and could be described approximately as

$$S = 1.23 - \frac{\Delta T}{385} \quad (0.23) \tag{15}$$

where ΔT is the amount of undercooling (Ref. 40). If we assume for the moment that this relationship is valid in our low gravity, high solidification rate experiment we can calculate an approximate degree of undercooling from our values of S. The values so calculated are shown in Table 5 and range from 50 to 135K. There are several reasons why this procedures may be inaccurate; these are discussed in Section IV.

IV. DISCUSSION

A. General Observations

One of the accomplishments of this experiment was to demonstrate the feasibility of using the drop tower to produce scientifically useful specimens of metals solidified in a low-gravity, low-pressure environment in a regular, rapid, repetitive, and cost-effective manner. The technique has not progressed to the point where we can control the temperature of superheat or the dwell time in the liquid state, but it is thought that changing the electrical characteristics of the power supply would result in a substantial improvement in this area, and even without this control useful data have been obtained.

Examination of the data on specimen yield in conjunction with the results of the computer model of the melting process has resulted in a significant advance in our understanding of the parameters controlling the wire melting process and, hence, the reliability and success rate of the experiment. The existing program is currently applicable to most metals and alloys and could easily be broadened to include other types of power supplies, most probably allowing us to select the electrical parameters needed to provide a predetermined amount of superheating and/or produce larger specimens.

The color film temperature measurement technique that was developed for this study has proven to be a very potent source of information. Quite apart from their value as thermal records, the films are of interest in following the chronology of the melting and sphere-forming process. They have allowed detection of certain problems in the melting process including hot spot formation, wire rupture due to excessive tension in the specimen mount, and wire accelerations due to thermal expansion. The temperature-time-position record that they yield is extremely valuable in interpreting the experiment and could not be obtained in any other manner. As an unfortunate corollary to the wealth of information they provide, the films require a great deal of analysis time; time which is not always available to a low-level research effort. Further, the technique is still not fully developed and the accuracy obtained does not approach its full potential. Significant improvement is still possible.

Our measurements of the lattice parameters of material solidified in low gravity show no significant differences from terrestrial samples. Considering the disparity on an atomic scale in the relative magnitudes of atomic bonding forces and gravitational forces, this is not an unexpected result and confirms previous work (Ref. 5). In addition to these lattice parameter measurements, the X-ray patterns were also useful to rapidly determine what phases were present. Low-gravity solidification did not seem to have perturbed the normal

transformation sequence of liquid → gamma → martensite in the Fe-Ni alloys. However, these alloys were not chosen to be located in critical areas of the phase diagram and thus are not thought to be optimum for uncovering any possible alterations of phase equilibria or transformation kinetics by gravity.

A perplexing result was our observation of some very short solidification times, shorter than can be accounted for by theory or previous experimental experience. A possible explanation for this behavior could be that the samples were not heated sufficiently to become fully molten. This is discounted on the basis of the microstructural observations; unmelted regions would be obvious, and we never observed microsturctures which could be interpreted as such. Also, as mentioned earlier, these short solidification times cannot be accounted for on the basis of bulk undercooling because they were measured from the instant of sphere formation, not from the length of the solidification plateau. We are unable to offer an explanation for these observations.

This experiment has further demonstrated the shortcomings of the naive notion that metallic specimens which solidify in low gravity will be spherical. Some specimens are spherical, but there are also several reasons why nonspherical shapes may be produced. We observed two phenomena leading to nonspherical morphologies (refer to Section III - external morphologies, overall shape). Others have been previously documented (Ref. 22).

Surface microstructure or microtopography is not usually an important consideration in metallic solidification. Most "as-cast" surfaces are formed by the mold wall and are machined or polished after solidification if the surface condition is important. A low-gravity environment allows containerless solidification, and the surface microstructures obtained will be controlled by surface tension, atmospheric contaminants, and the solidification process. There is little prior experience in this domain, and if technology ever progresses to the point of seriously considering containerless casting there will be a need for an understanding of the possibilities. Our somewhat haphazard investigation of surface microstructures has shown that a variety of structures occurs and, in some cases, features are generated which are visible to the naked eye. Defects such as pores are not uncommon; some form of control would be required in order to guarantee good quality surfaces.

We might use these surface microstructures as a record of containerless solidification. Most of the observations are understandable in a straightforward manner, the most potent phenomena being shrinkage feeding and evaporation. The blocky faceted structures (Fig. 21 and 22) that we explained as due to oxide solidification seem unique and worthy of further study. Little or no information is available on low-gravity solidification of these compounds.

The "buttes" (Fig. 23 and 24) are very perplexing structures; in principle, any of the explanations advanced in Section III (external morphogies, surface microstructures) are possible. Controlled experiments would be necessary to arrive at a sound understanding of the phenomena.

The cross-sectional microstructures are exactly as would have been predicted with the exception of one point. The observed microstructures were always very fine-grained and equiaxed; this was true for all of the specimens examined and includes pure nickel, Ni-5% Al (two batches), Fe-15% Ni, Fe-26% Ni, and W-25% Re. This result was not anticipated and is difficult to explain. Previous work on castings of Fe-25% Ni has shown that this alloy solidifies dendritically even when chill cast so as to keep the solidification times very short, as short as the times involved in this experiment (Ref. 16, p. 149). Further, it has previously been established that grain morphology is independent of solidification times (Ref. 16, p. 148). Equiaxed morphologies are observed only in the case of Fe-25% Ni castings undercooled by more than 170 K. Dendritic morphologies are also observed in atomized superalloy powders (Ref. 15). These powders were solidified in free fall and under heat extraction conditions very similar to ours. The superalloys should have similar heat conductivity but a broader freezing range than the Fe-25% Ni. A narrower freezing range will favor columnar rather than equiaxed structures under otherwise identical conditions (Ref. 16).

It is not clear from the etching behavior if these are equiaxed dendrites, albeit very fine and with a spherical grain morphology, or if they are truly nondendritic structures such as observed in zirconium inoculated magnesium castings. Further experiments would be required to establish this point (Ref. 16).

If we rule out the possibility that these specimens were undercooled by more than 170 K (as discussed in Section IV - undercooling), we must explain the equiaxed structure in terms of a greatly enhanced nucleation rate. Three possible explanations for an enhanced nucleation rate are cavitation, convection, or inoculation.

Fluid mechanical cavitation is often advanced as an explanation for the 175 K morphological transition in undercooled castings (Ref 16). It is thought that the rapid fluid flow required to feed the solidification shrinkage causes bubble formation; subsequent collapse of the bubble generates pressures high enough to cause nucleation. There is also the possibility of inducing cavitation by external means, i.e., by vibration or shock. In a low-gravity environment the lack of a pressure head will allow cavitation to occur more easily; unanticipated thermal cavitation of metallic melts was observed in some Skylab experiments

(Ref. 22). We think it unlikely (although possible) that our wire melting process could produce an external stimulus (e.g., shock wave or vibration) violent enough to cause cavitation. However, it is possible that the same process which gives rise to the 175 K morphological transistion is causing our equiaxed structures. Assuming that the 175 K transition is due to cavitation that occurs at some critical rate of interface motion, it follows that the critical rate of interface motion required to induce cavitation will be lower in a low-gravity environment. Since the dendrite tip velocity, R, is related to the undercooling, ΔT, by

$$R = a\Delta T^n \tag{16}$$

where a is a constant and n is approximately 2 (Ref. 16) we see that if fluid mechanical cavitation is the cause, then the morphological transition should occur at a smaller ΔT in low gravity. We think that small undercoolings occur in many of our specimens (refer to Section IV - undercooling). Thus, this is one possible explanation for the equiaxed structures and, if correct, these structures are a direct consequence of the low-gravity environment.

Convection has been shown to have different effects on the structure of castings. On the one hand, Cole and Bolling (Ref. 41) have shown that reduced convection can eliminate the equiaxed zone in castings; whereas it has also been shown (Ref. 16) that convection is necessary for the formation of the equiaxed chill zone. Fluid motion certainly occurs in our sphere-forming experiment; however, observations on some specimens formed from wires with pronounced surface features lead us to conclude that the fluid motion is not particularly vigorous. Thus, we tend to discount the effect of convection.

Inoculation by some unknown impurity is also discounted because the alloys used were of various purity levels and because all the different alloys showed the same equiaxed morphology. We are left with a final hypothesis, namely, that of self-seeding by small unmelted crystallites. We know that no large ($>1\,\mu$m) particles remained unmelted because they would have been visible in the optical microstructures. However, it is possible that because of our short dwell times in the liquid state, small ($\simeq 10$ nm) crystallites could have remained unmelted. These crystallites would easily be capable of serving as nuclei for solidification. This explanation is not wholly satisfactory because the temperature-time record almost invariably shows a reading well above the melting point. For the moment, we can offer no conclusions in this regard.

B. Undercooling

To observe bulk undercooling in liquid melts, one must continuously measure the temperature of the melt and show that solidification does not begin until some temperature

below the equilibrium solidification temperature. In this experiment we have not been able to demonstrate bulk undercooling in this manner. None of our temperature-time histories show unequivocally the occurrence of bulk undercooling. Unfortunately, the film technique of temperature measurement is very time consuming and of somewhat variable accuracy. Due to limitations of time, we have not been able to analyze films of all the drop tests and some of the analyzed films gave rise to data of dubious value. Thus, on this basis, we have not observed undercooling in low-gravity.

Due to the incomplete and unreliable nature of the temperature measurements we have also sought other, secondary, evidence of bulk undercooling. These secondary parameters have been previously shown to be functions of the degree of undercooling and include grain morphology, segregation ratio, solute distribution, and solidification time. We will briefly discuss each of these parameters.

It has been observed that the grain morphology of Fe-Ni castings changes from dendritic to equiaxed for $\Delta T > 170$ K (Ref. 39, 40, 34). All of our microstructures were equiaxed; thus, this observation indicates consistent high degrees of undercooling. It should be mentioned that the grain size or dendrite element spacing was shown to be a function of solidification time independent of morphology, i.e., dendritic and equiaxed structures fall on the same curve (Ref. 34).

The segregation ratio, S, has been shown to decrease with increasing undercooling as discussed in Section III - solute redistribution, localized (Ref. 40). On the basis of measured segregation ratios, our Fe-26% Ni specimens were undercooled from 50 to 135 K as shown in Table 5.

Previous studies (Ref. 39) have shown that in highly undercooled melts of Fe-Ni the first solid is formed by a diffusionless mechanism; thus, high-solute cores should be observed. None of our microprobe traces showed evidence of high solute cores. Occasional etched structures were obtained that could be interpreted as high-solute cores, e.g., Fig. 26 and 27, but no consistent trend was noticed. Thus, this phenomenon indicates little or no undercooling.

Where it is defined as the length of the constant temperature plateau, the solidification time is inversely proportional to the degree of undercooling. Unfortunately, the solidification times reported in Table 2 are measured from the wire break to the end of the constant-temperature plateau. Thus, they are unaffected by undercooling and provide no further information.

In summary, these secondary "measures" of undercooling provide inconsistent indications of the degree of undercooling. The absence of high-solute cores indicates little or no undercooling, while the spherical grain morphology is associated with $\Delta T > 170$ K and the segregation ratio indicates $\Delta T \approx 100$K. Since these are all secondary or derived measurements and because the effects of undercooling on microstructure and solute distribution are not fully understood, we must conclude that there is no legitimate basis for assuming that consistent pronounced undercooling has occurred. In spite of this conclusion, we note that the results are perplexing and worthy of further study, particularly with regard to how gravity may have altered the relationships between the different microstructural effects of undercooling.

C. Evaporative Segregation

Taken in the context of our experimental conditions that include an uncontrolled and unknown time-temperature history during the interval when the specimen is molten, our results on evaporative segregation demonstrate the variable and unpredictable nature of this phenomenon.

In the case of Ni-Al, the results seemed to confirm theoretical predictions although neither the predictions nor the results were very clear-cut. In the case of Fe-Ni, the difference in evaporation rates were too small to give rise to measurable segregation; whereas, in the case of Fe-C, our observations were opposite to predictions but easily explained on the basis of an oxidation reaction at the surface of the specimen. Further, in all cases, it was observed that the amount of solute redistribution due to solidification was greater than or equal to the total amount of redistribution due to evaporation. This is a consequence of our very short dwell times in the liquid state and should be considered more as a limitation of the experimental technique than as a limitation on the process of evaporative purification. However, these two observations demonstrate that other competitive and potent segregation phenomena exist and must be considered ir any contemplated purification process.

V. CONCLUSIONS

1. The wire-melting drop-test apparatus is a useful tool for rapid, cost-effective low-gravity research.

2. An alternative power supply (e.g., capacitor discharge) would extend the capabilities of the apparatus and allow greater control of superheat.

3. Computer modeling of the melting process allows rapid examination of the controlling parameters.

4. Observed solidification times can be significantly shorter than predicted.

5. Alloys of Fe-Ni and Ni-5% Al solidified at 10^{-4} g have the same lattice parameters as those solidified in one-g.

6. Low-gravity solidification does not perturb the normal transformation sequence of Fe-Ni alloys.

7. A perfect sphere is not always the most probable shape for a metal droplet solidified in low gravity.

8. Uncontained solidification of metals and metallic oxides leads to unusual surface microstructures and topographic features, many of which are explainable as last liquid effects, shrinkage feeding, and evaporation. The orgins of some of the observed surface microstructures are unclear.

9. Very fine-grained equiaxed structures were observed in all the specimens examined; no entirely satisfactory explanation can be given.

10. Large ($\Delta T > 170$ K) spontaneous undercoolings have not been observed, but the relationships between ΔT, grain morphology, grain size, segregation ratio, and solidification time seem to be perturbed by low-gravity solidification.

11. Evaporative segregation can occur to the extent predicted; theoretically, however, surface reactions and redistribution of solute during solidification can overwhelm and reverse these effects.

VI. SUGGESTIONS FOR FUTURE WORK

1. A new, controllable, melting power supply would greatly increase the utility of the apparatus and possibly allow resolution of many of the anomalous effects noted in this study, some of which are suspected of being equipment related.

2. Automation of film scanning and data analysis would greatly enhance the utility of the temperature measurements by allowing more extensive and more accurate readings of the films.

3. The short solidification times should be studied, possibly by variation of superheat temperatures.

4. The uncontained low-gravity solidification of metallic oxides seems worthwhile for future study, perhaps with a view towards producing unique as-cast shapes.

5. A study of surface microstructures obtained by containerless solidification in various atmospheres may lead to a capability for producing useful and/or unique as-cast features.

6. A study of the reasons for the occurrence of very fine-grained equiaxed structures in low-gravity solidification would be very desirable; this is probably the single most important phenomenon for future work.

7. A parametric investigation of the effect of undercooling on microstructural features in low-gravity solidification will be of scientific and technical interest.

8. Longer, more controlled investigation of evaporative purification in a variety of systems would be required to demonstrate the utility of this phenomenon.

VII. ACKNOWLEDGEMENTS

It is a pleasure to acknowledge the continued encouragement and assistance of Leroy H. Berge, our Contract Monitor. Our visits to the MSFC tower were successful largely due to Roy's enthusiasm and to the very capable support of Hugh Feather and his team of technicians.

Professor T. Z. Kattamis kindly provided Ni-5% Al wire and served as a consultant; we appreciate his valuable advice and his review of the manuscript. Dr. P. Wasilewski of NASA - GSFC provided all of the Fe-Ni alloys used in this project.

We wish to thank Mr. G. Busch of the Grumman Research Department for providing the microprobe analyses.

M. Kesselman and E. Kennelly of the Grumman Research Department were always helpful when we encountered equipment problems, and M. Kesselman and R. Misita are responsible for the computer modeling work. The continued advice and encouragement of W. Aubin and G. Geschwind are sincerely appreciated. Finally, W. Poit literally braved December's ice and January's cold to successfully perform these experiments under very difficult conditions.

VII. REFERENCES

1. Proceedings, Third Space Processing Symposium, Skylab Results vols. 1 and 2, NASA, Marshall Space Flight Center, June 1974. Available from N. T. I. S., Springfield, Va. 22151.

2. Lorenz, A., "Geplante Anlage Fur Versuche Unter Schwerelosigkeit" DFVLR - Nachrichten 14, 563, July 1974.

3. Zenkevich, V. B., "On the Behavior of a Liquid Under Conditions of Weightlessness," Teplofizika Vysokikh Temperatur, 2 no. 2, pp. 230-237, 1964, (in Russian).

4. Report of the USRA Committee, coordinated by H. Leidheiser, Jr., April 15, 1974.

5. Aubin, W. M., Larson, Jr., D., and Geschwind, G. I., "Research of Metal Solidification in Zero-G State," Final Report on contract NAS 8-28604, Grumman Research Dept. Memorandum RM-544, September 1973.

6. Busch, G. and Hilgeman T., "A Photographic Technique for Measuring Temperatures," Grumman Research Dept. Memorandum RM-580, October 1973.

7. Handbook of Chemistry and Physics, Chemical Rubber Publishing Co., Cleveland, Ohio, 39 ed., p. 2752, 1958.

8. DeCarlo, J. and Hilgeman, T., Grumman Research Department, to be published, 1975.

9. Kesselman, M. and Misita, R., "XPLOD," Grumman Aerospace Corp., Research Dept., 1975.

10. Gandolfi, G., "Discussion upon Methods to Obtain X-ray Powder Patterns from a Single Crystal," Miner. Petrogr. Acta, 13, pp. 67-74, 1967.

11. Steurer, W. H. and Gorham, D. J., "Processes for Space Manufacturing," Final Report on NASA contract NAS8-24979, General Dynamics Report No. GDC-DBG70-001, June 1970.

12. Paynter, H. L., AIAA Jour., 2, 1624, 1964.

13. Exploding Wires, Plenum Press, Inc., New York, vol. 2, 1962; vol. 3, 1964.

14. Li, C. H., "Evaporation in Space Manufacturing," AIAA/ASME, Thermophysics and Heat Transfer Conference, AIAA paper no. 74-667, 1974.

15. Joly, P. A., and Mehrabian, R., J. Mater. Sci., 9, 1446, 1974.

16. Flemmings, M. C., Solidification Processing, McGraw Hill, New York, 1974.

17. Reichman, J., "Solidification of Molten Metal Spheres in a Vacuum," Grumman Research Dept. Memorandum RM-544, 1972.

18. Dushman, S., Scientific Foundation of Vacuum Technique, John Wiley & Sons, Inc., 2nd edition, 1962.

19. Rohsenow, W. M. and Hartnett, J. P., Handbook of Heat Transfer, McGraw Hill, New York, p. 9-7, 1973.

20. Touloukian, Y. S. and DeWitt, D. P., Thermal Properties of Matter, IFI/Plenum, New York, 1970.

21. Culity, B. D., Elements of X-Ray Diffraction, Addison-Wesley, Reading, Mass. 1956.

22. Larson, Jr., D. J., "Specimen Analysis of Skylab, M533 Experiment, Flight Specimens," Final Report on Phase C Contract NAS 8-28728, Grumman Research Department, Report RE-486, 1974.

23. Zwell, L., Carnahan, D. E., and Speich, G. R., Met Trans. 1, 1007, 1970.

24. Bo[illegible]tinger, W. J., Met. Trans., 5, 2023, 1974.

25. Titchener, A. P. and Spittle, J. A., Acta Met, 23, 497, 1975.

26. Hirth, J. P. and Pound, [illegible] M., "Condensation and Evaporation," Progress in Materials Science, ed. B. Chalmers, vol. 11, p. 145, 1963.

27. Magee, C. L. and Davies, R. G., Acta Met, 19, 345, 1971.

28. Carruthers, J., Bell Laboratories, Murray Hill, N. J., private communication.

29. Pearson, J. R. A., J. Fluid Mech., 4, 489, 1958.

30. Hultgren, R., Desai, P., Hawkins, D., Gleiser, M., Kelley, K., and Wagman, D., Selected Values of the Thermodynamic Properties of The Elements, American Society for Metals, Metals Park, Ohio, 1973

31. Scriven, L. E. and Sternling, C.V., J. Fluid Mech, 19, 321, 1964.

32. Jones, H. and Leak, G. M., Metal Sci. J., 1, [illegible]11, 1967.

33. Hilgeman, T., Grumman Research Depart[illegible], private communication.

34. Kattamis, T. Z. and Flemmings, M. C., Trans. TMS-AIME, 236, 1523, 1966.

35. Richardson, F. D., Physical Chemistry of Melts in Metallurgy, Academic Press, London, 1974.

36. Baker, L. A., Warner, N. A., and Jenkins, A. E., Trans. TMS-AIME, 239, 857, 1967.

37. Lord, A. E. and Beshers, D. N., Acta Met, 14, 1659, 1966.

38. Beaman, D. R. and Isasi, J. A., Electron Beam Microanalysis, ASTM, STP 506, Philadelphia, 1972.

39. Kattamis, T. Z., Z. Metalkde, 61, 856, 1970.

40. Kattamis, T. Z. and Flemmings, M. C., Mod. Casting, 52, 191, 1967.

41. Cole, G. S. and Bolling, G. S., Trans TMS-AIME, 239, 1824, 1967.